ACS Catalysis

pubs.acs.org/acscatalysis Research Article

Electrocatalytic Hydrogen Evolution and Oxidation with Rhenium Tris(thiolate) Complexes: A Competition between Rhenium and Sulfur for Electrons and Protons

Hao Tang, Edward N. Brothers, Craig A. Grapperhaus,* and Michael B. Hall*

Cite This: *ACS Catal.* 2020, 10, 3778−3789 Read Online

ABSTRACT: Recent electrochemical experiments reveal that the rhenium-tris(thiolate) [**ReL**$_3$] (L = DPPBT = diphenylphosphinobenzenethiolate, a noninnocent ligand) complex catalytically reduces protons and oxidizes H_2 (*J. Am. Chem. Soc.* **2015**, *137*, 9238). Direct calculations of redox potentials (E^0), acidity constants (pK_a), and free energies of activation ($\Delta G^{\ddagger}$) by density functional theory (DFT) with the help of high-level *ab initio* calculations predict that hydrogen oxidation reaction (HOR) thermodynamically and kinetically favors a Re-hydride/monothiol intermediate, while the hydrogen evolving reaction (HER) favors Re-dihydride intermediates, in contrast to the Re-dithiols as proposed previously. The catalytic pathway for HOR involves two oxidation steps from [**ReL**$_3$] to [**ReL**$_3$]$^{2+}$, followed by H_2 addition to form the Re-hydride/thiol, [(**ReH**)(**S**$_1$**H**)**L**$_2$]$^{2+}$. Under basic conditions, deprotonation of this complex produces [**Re**(**S**$_1$**H**)**L**$_2$]$^+$ with the thiol as S1, rather than the proposed S3. Further deprotonation of [**Re**(**S**$_1$**H**)**L**$_2$]$^+$ closes the catalytic cycle to regenerate [**ReL**$_3$]. For the HER, DFT calculations predict that [**ReL**$_3$] is reduced to [**ReL**$_3$]$^-$, followed by protonation of [**ReL**$_3$]$^-$ at the Re center to produce metal-protonated [(**ReH**)**L**$_3$] in accordance with the E^0 = −1.45/−1.60 V (cal./exp.). The E^0 calculations suggest a reassignment of the experimentally observed peak at −1.70 V to the singly protonated E([**ReL**$_3$·**H**]$^{0/-}$) rather than the doubly protonated E([**ReL**$_3$·**H**$_2$]$^{+/0}$). This reassignment and the low relative pK_a's of [**ReL**$_3$·**H**$_2$]$^+$ illustrate that addition of the second proton must follow the second electrochemical reduction of [(**ReH**)**L**$_3$] to [(**ReH**)**L**$_3$]$^-$, which is basic enough to be protonated at the Re center making the formation of the Re-dihydride [(**HReH**)**L**$_3$]. Production of H_2 occurs via reductive elimination through a Re−H_2 adduct. The nature of the key intermediates from the DFT calculations is confirmed by the complete active space calculations (CASSCF). This comprehensive investigation into the HOR and HER mechanisms can guide further experimental and theoretical efforts on rationally designing the effective electrocatalysts by comparing how various ligand modifications may shift the mechanistic steps.

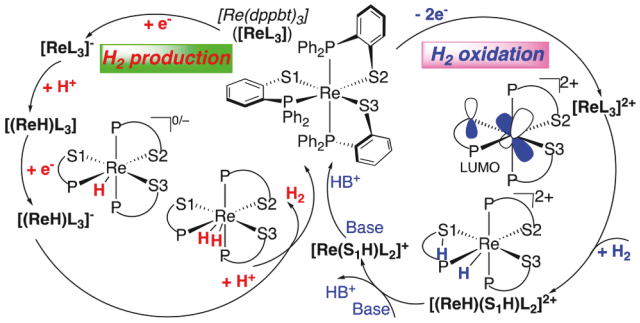

KEYWORDS: *density functional theory, noninnocent ligand, hydrogen oxidation, proton reduction, rhenium-tris(thiolate) complex, electrochemical reduction, redox potentials, complete active space calculations*

1. INTRODUCTION

Interest in efficient generation and storage of energy from renewable resources instead of fossil fuels has increased dramatically.[1] The use of H_2 in fuel cells is an attractive strategy in this field.[2] Inspired by the H_2 oxidation and H_2 production catalyzed in nature by [FeFe]- and [NiFe]-hydrogenases,[3] a wide variety of molecular catalysts have been designed and investigated as electrocatalysts for hydrogen evolution reaction (HER),[4−8] including Co-,[5] Ni-,[6] Fe-,[7] and Cu-based[8] complexes. These catalysts have been extensively explored both experimentally and computationally.[4−8]

Dithiolene ligands have recently attracted tremendous interest in the design of effective HER electrocatalysts because the ligands are both redox-active, which allows for the storage of reducing equivalents, and the sulfur atoms may serve as proton relays.[9] The potential utility of such catalysts is reflected by recent studies on the cobalt[10] and nickel dithiolenes[11] as photocatalysts or electrocatalysts for proton reduction.

Most recently, a proposed ligand-centered electrocatalytic H_2 oxidation and production based on the synthetic mononuclear Re-tris(thiolate) complex [Re(DPPBT)$_3$] (DPPBT = diphenylphosphinobenzenethiolate) (denoted as [**ReL**$_3$]) has been reported.[12] It is expected that the

Received: October 23, 2019
Revised: February 20, 2020
Published: February 21, 2020

   https://dx.doi.org/10.1021/acscatal.9b04579
ACS Catal. 2020, 10, 3778−3789

noninnocent character of the DPPBT ligand, which has the ability to delocalize electron density like dithiolenes,[13,14] may play important roles in these reactions. However, the details of the mechanisms for H_2 oxidation and evolution catalyzed by [**ReL**$_3$] and the nature of the H_2 evolving complex and the H_2 addition complex are still unclear, although ligand-centered reactivity was suggested based on similarities to the redox-regulated, ligand-based addition of ethylene to [**ReL**$_3$].[15] In the originally proposed mechanism for the H_2 oxidation reaction (HOR), as shown in Scheme 1 (blue), [**ReL**$_3$] was oxidized by

Scheme 1. Proposed Electrocatalytic Cycles for H_2 Oxidation and H_2 Evolution with Catalyst [ReL$_3$]

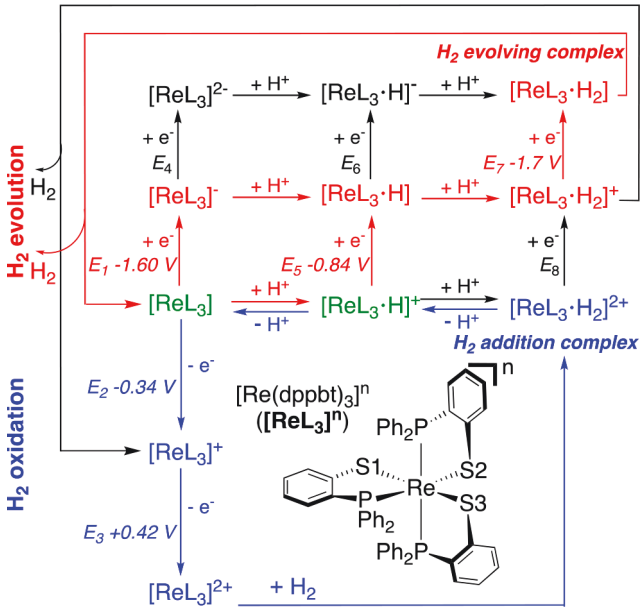

two electrons and then H_2 adds to yield the hydrogen addition complex, [**ReL**$_3$**·H**$_2$]$^{2+}$. Stepwise deprotonation with two equivalents of triethylamine regenerates [**ReL**$_3$] via [**ReL**$_3$**·H**]$^+$, in which the ligand S3 is the thiol. Its reduced derivative [**ReL**$_3$**·H**] has been observed as a pink species in solution but has not yet been isolated. For H_2 production, the cyclic voltammetry supported competing CECE and ECCE mechanisms for catalysis as shown in Scheme 1 (red). The CECE mechanism begins with protonation of [**ReL**$_3$], then one−electron reduction, then a second protonation, and finally the second one-electron reduction before H_2 loss. The ECCE mechanism involves the one−electron reduction of [**ReL**$_3$] to [**ReL**$_3$]$^-$ prior to the first protonation, then a subsequent second protonation, and reduction before H_2 loss. In addition to the CECE and ECCE mechanisms, experimentalists proposed that alternative catalytic cycles for HER such as EECC, CEEC, ECEC, and CCEE should be considered for completeness (Scheme 1 (black)).

In this paper, the full catalytic cycles for electrocatalytic H_2 oxidation and H_2 production catalyzed by [**ReL**$_3$] are investigated by using DFT and higher-level *ab initio* calculations. Our previous DFT and CASSCF calculations showed that [**ReL**$_3$]^n (n = 0, +, and 2+) complexes have mixed metal−ligand character in the frontier orbitals and have some multireference character, especially the more oxidized ones.[14b] Such noninnocence portends H_2 addition, protonation, and redox on any of the S ligands (S1, S2, and S3) or at Re.[14b] Therefore, we examine all the possibilities for H_2 addition, protonation, in a variety of redox states for the various species occurring in the proposed mechanisms for H_2 oxidation and H_2 production. To establish the validity of the mechanisms for the HOR and HER, we calculated the thermodynamic data including the reduction potentials (E^0) and relative pK_a's and kinetic data including free energy barriers along the various mechanistic pathways. In addition to DFT calculations, high level *ab initio* methods including coupled cluster CCSD(T)[16] and complete-active-space self-consistent-field (CASSCF)[17] were employed to identify the most thermodynamically stable species and elucidate the accurate electronic structure of the key intermediates involved in the catalytic cycles.

2. COMPUTATIONAL METHODS

DFT calculations were performed by using the Gaussian 09 suite of program.[18] Benchmarking studies with 15 different functionals, including B97D,[19] M06L,[20] BP86,[19,21] TPSS,[22] TPSSh,[22] ω-B97X,[23] ω-B97XD,[24] B3LYP,[19,21a,b] B3P86,[19,21c] B3PW91,[25] PBE0,[26] MN12SX,[27] M06,[20,28] BMK,[29] and BHandHLYP,[18] are shown in the Supporting Information (SI). The M06 functional affords relative free energies, structures, and reduction potentials of the more reduced [**ReL**$_3$]$^{0/-}$ and [**ReL**$_3$]$^{+/0}$ couples that are consistent with available experimental values (Tables S1−S9), while the B3PW91 functional is found to be more accurate for the redox potential calculations of the more oxidized [**ReL**$_3$]$^{2+/+}$ couple (Table S9). Moreover, M06 was found to reproduce the experimentally observed activation barriers for the addition and loss reactions of [**ReL**$_3$]$^+$ with ethylene very well from the experimental values (root-mean-square deviations less than 2 kcal/mol). For these reasons, both M06 and B3PW91 functionals were used for the DFT calculations.

The geometric structures of all the species were optimized in the gas phase (GP). The LANL2DZ basis set[30] with ECP was used for Re, the 6-31G(d) basis set was used for atoms bonded to Re (C, P, S, and H atoms) and the substrate H_2 molecules, and 6-31G was used for all other atoms (C and H atoms on phenyl group). This mixed basis set (denoted as B1) was tested and found to be an acceptable compromise between cost and accuracy. Frequency analysis was conducted at the same level to verify the nature of all intermediates (no imaginary frequency) and transition state structures (only one imaginary frequency) and to obtain the thermodynamic energy corrections. The transition state structures were also confirmed to connect reactants and products by intrinsic reaction coordinate (IRC) calculations. The gas-phase free energies were calculated at T = 298.15 K. Solvation effects in dichloromethane were taken into account by single point calculations on gas-phase optimized structures using the continuum solvation model SMD.[31] The electronic energies were recomputed with the same functional using the larger basis sets: SDD(f)[32] (Re), 6-311++G** (C, P, S, and H atoms), and 6-31G* (C and H atoms on phenyl group) (denoted as B2). DFT empirical dispersion corrections[33] were employed in the single-point calculations, wherein DFT-D3 with BJ damping was used for the B3PW91 functional and DFT-D3 with zero damping was used for the M06 functional. To examine if the solvent would cause any significant energetic or geometric changes in species with high charges, the geometries of [**ReL**$_3$]$^{0/+/2+}$ and the ligand-monoprotonated [**Re(LH)L**$_2$]$^{+/0}$ were reoptimized in solvent with M06-L, TPSS, B3P86, M06, B3PW91, PBE0, and ω-B97XD func-

https://dx.doi.org/10.1021/acscatal.9b04579
ACS Catal. 2020, 10, 3778−3789

tionals in combination with basis set B2. The resulting energetic gaps between the low- and high-spin states, geometrical parameters, and redox potentials matched those based on DFT/B2/SMD//DFT/B1/GP calculations, respectively (Tables S1−S9). Both M06 and B3PW91 predict similar trends for the possible pathways for the HOR. Moreover, the B3PW91 functional was found to perform better for the redox potential calculations for the cation and dication $[\mathbf{ReL_3}]^{+/2+}$ that are involved in the HOR. Thus, herein we mainly discuss the HOR free energy profile obtained at the B3PW91-D3/B2/SMD//B3PW91/B1/GP level, while the HOR free energy profile calculated at the M06-D3/B2/SMD//M06/B1/GP level is displayed in Figure S3. The data for the HER was reported in the text at the M06-D3/B2/SMD//M06/B1/GP level.

Reduction potentials were calculated from $\Delta G^\circ = -nFE^0$, where n is the number of transferring electrons, F is Faraday's constant, and ΔG° is the free energy of reduction with 1 M standard states. All reduction potentials were determined with respect to the ferrocenium/ferrocene couple (Fc^+/Fc) in dichloromethane. The equation $\Delta G^\circ = -[\ln(10)RT]pK_a$ was used to calculate pK_a's, where ΔG° is the free energy of protonation. We report ΔpK_a's relative to calculations on acetic acid as a reference because it was used in the experimental studies.

***Ab Initio* Calculations.** High-level *ab initio* CCSD(T) and CASSCF single-point calculations were carried out with the MOLPRO suite of programs[34] by using the basis set SDD(f)(Re)/6-311G* (other atoms) (B3) at the DFT-(M06)-optimized geometries. To reduce the computational cost of the high-level *ab initio* methods for the full-ligand systems: $[\mathbf{ReL_3}]^{-/0/+/2+}$, $[\mathbf{ReL_3{\cdot}H}]^{+/0/-}$, and $[\mathbf{ReL_3{\cdot}H_2}]^{0/+/2+}$, the ligand was truncated (denoted **L′**) as successfully employed in our previous studies of $[\mathbf{RuL_3}]^+$ and $[\mathbf{ReL_3}]^{0/+/2+}$.[14] For DFT calculations on the truncated models, geometries, frequencies, and free energies at 298.15 K were computed using the M06 functional in combination with basis set B3. The single-point calculations were performed with the SDD(f)(Re)/6-311++G**(rest) basis set (B4) with the same M06 functional based on the optimized structures. The continuum solvation model and solvent were the same as those for the full-ligand molecules. The comparisons of the relative energies and geometries between the full ligand and the truncated modes are collected in Figures S1−S2 and Tables S10−S11.

To examine the accuracy of the DFT electronic structures of the key intermediates that are involved in the catalytic cycles of H_2 oxidation and H_2 production, we performed CASSCF calculations on the corresponding truncated models. The CASSCF calculations show that most of these species have small multireference character, as indicated by the small weight (less than 2.6%) of the second most important configurations (Figures S26−S39, Tables S23−S36), such that the DFT results should not suffer from any near-degeneracy problems.

3. RESULTS AND DISCUSSION

Structures and Energies of $[\mathbf{ReL_3}]^{-/0/+/2+}$. Figure 1 shows the key geometric parameters and relative free energies for the $[\mathbf{ReL_3}]^{-/0/+/2+}$ species in the low and high spin states. As in our previous study,[14b] DFT calculations show that the low spin states are thermodynamically favored for all the species $[\mathbf{ReL_3}]^{-/0/+/2+}$, wherein the anion, cation, and dication $[\mathbf{ReL_3}]^{-/+/2+}$ have larger gaps between the low and high spin

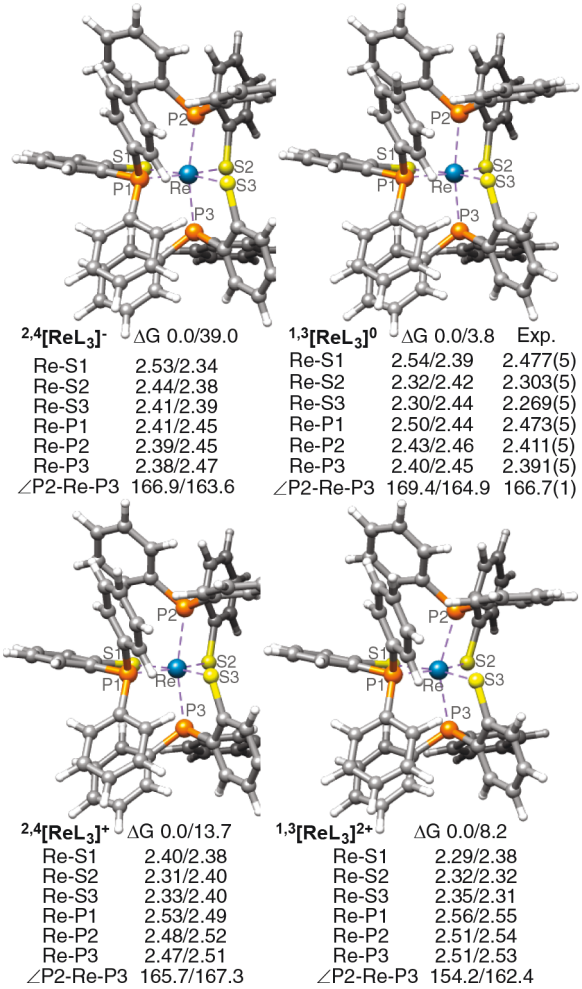

Figure 1. M06-optimized geometric parameters (bond lengths in Å and angle in deg) and relative free energies (in kcal/mol) of $[\mathbf{ReL_3}]^{-/0/+/2+}$ for the low- and high-spin states.

states than the neutral $[\mathbf{ReL_3}]$, which has a closely lying $S = 1$ state. Like DFT, the higher-order methods, CCSD(T) and CASPT2 calculations, predict that the singlet state of $[\mathbf{ReL_3}]$ is 8.5 and 24.5 kcal/mol lower than the triplet state, respectively. The optimized Re−S and Re−P bond lengths for $[\mathbf{ReL_3}]$ agree with those of the crystal structure[12] for the singlet state within 0.06 Å.

As shown in Figure 2, reduction of $[\mathbf{ReL_3}]$ to $[\mathbf{ReL_3}]^-$ generates the low-energy doublet state with one electron in the π^*_{xz} orbital, which is mainly localized on the Re center as reflected by the Mulliken spin populations of $\rho_{Re} \approx 0.80$, $\rho_{S1} \approx 0.00$, $\rho_{S2} \approx 0.07$, and $\rho_{S3} \approx 0.08$, respectively (Figure 2a), like the previous work.[12b] Oxidation of $[\mathbf{ReL_3}]$ produces $[\mathbf{ReL_3}]^+$ in a low-energy doublet state with one electron in the π^*_{yz} orbital, which is delocalized between Re and S1 with the Mulliken spin populations of $\rho_{Re} \approx 0.66$, $\rho_{S1} \approx 0.30$, $\rho_{S2} \approx -0.03$, and $\rho_{S3} \approx -0.03$, respectively (Figure 2c). Further oxidation to $[\mathbf{ReL_3}]^{2+}$ removes the remaining electron from the π^*_{yz}, yielding a singlet ground state (Figure 2d). In accord with the nature of the π^*_{yz}, which is antibonding between the Re-d_{yz} and S1-p_y orbitals, the Re−S1 bond distance progressively shortens in the low-spin state from neutral to dication (Figure 1). The details of the electronic structures of the Re-tris(thiolate) complexes $[\mathbf{ReL_3}]^{0/+/2+}$ were reported by our previous DFT and CASSCF work.[14b] CASSCF calculations

https://dx.doi.org/10.1021/acscatal.9b04579
ACS Catal. 2020, 10, 3778−3789

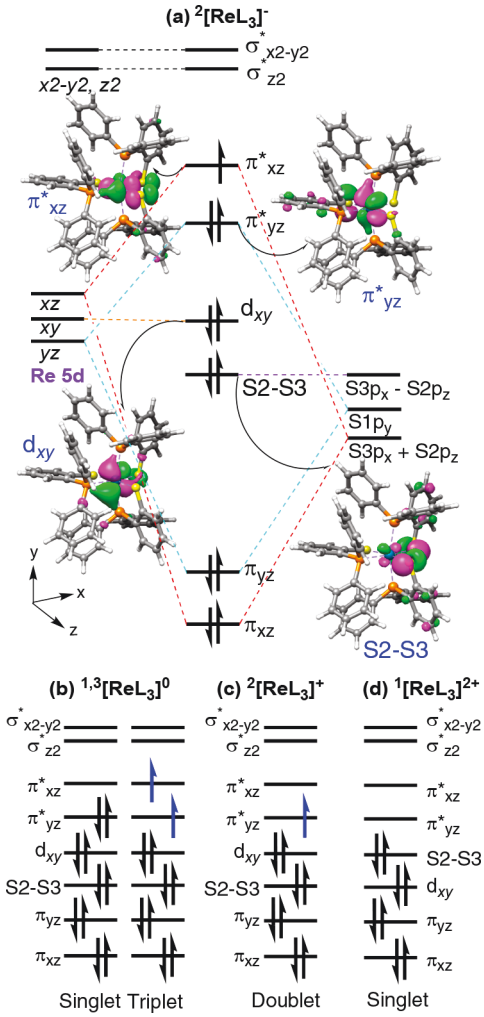

Figure 2. Schematic DFT MO diagrams for $[\mathbf{ReL_3}]^{-/0/+/2+}$.

reveal that the neutral species $[\mathbf{ReL_3}]^0$ is well-described as a closed-shell singlet ground state involving a Re(III) (d^4, S = 0) bound to three thiolate-DPPBT ligands. In contrast, the oxidized derivatives $[\mathbf{ReL_3}]^+$ and $[\mathbf{ReL_3}]^{2+}$ have major contributions from Re(III) (d^4, S = 1) antiferromagnetically coupled to one thiyl- with two thiolate-DPPBT ligands for $[\mathbf{ReL_3}]^+$ and to two thiyl- with one thiolate-DPPBT ligand for $[\mathbf{ReL_3}]^{2+}$. Although CASSCF calculations predict that most of the key intermediates have some multireference character, they are not enough to cause concern about near degeneracy problems.[14]

H_2 Oxidation Mechanism. Since H_2 oxidation begins with H_2 addition to $[\mathbf{ReL_3}]^{2+}$, we examined all the possibilities for the structure of $[\mathbf{ReL_3{\cdot}H_2}]^{2+}$, with the likely protonated sites in each ligand (S1, S2, and S3) or metal as well as their stereoisomers. The most stable adducts are shown in Scheme 2: the ligand-centered adducts $[\mathrm{Re}(\mathbf{LH})_2\mathrm{L}]^{2+}$ (**1**−**3**), the metal and ligand-based adducts $[(\mathbf{ReH})(\mathbf{LH})\mathrm{L}_2]^{2+}$ (**4**−**6**), and metal-based adducts $[(\mathbf{HReH})\mathrm{L}_3]^{2+}$ (**7**, **7′**, **7″**, **8**, and **8′**).

Figure 3 shows the free-energy pathways on the singlet (ground state) for H_2 oxidation by $[\mathbf{ReL_3}]^{2+}$ to yield the corresponding conformers in Scheme 2. As shown in Figure 3, when H_2 approaches $[\mathbf{ReL_3}]^{2+}$, the Re-dihydrogen complexes (**7**, **7′**, and **7″**) with various H_2 orientations are formed first; then, the H−H bond cleaves either heterolytically or homolytically. Specifically, the H−H bond in the Re-

Scheme 2. H_2 Addition to $[\mathbf{ReL_3}]^{2+}$ to Form Different H_2 Addition Conformers: (a) Ligand S and S Based Addition; (b) Metal and Ligand Based Addition; and (c) Metal Based Addition

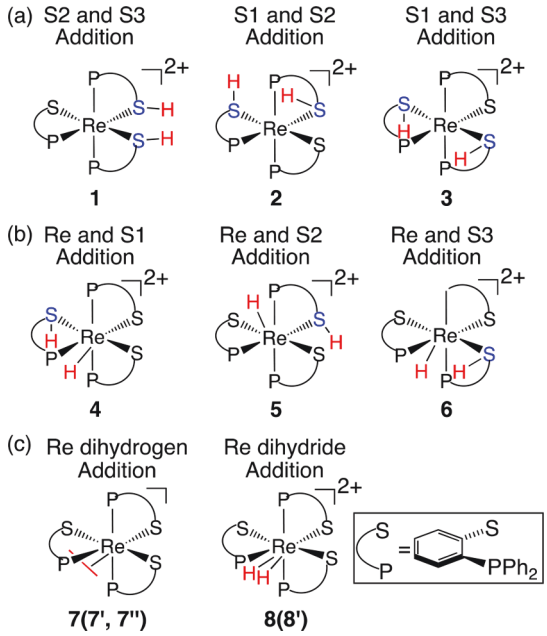

dihydrogen (**7″**) can be split heterolytically by Re and S1 (acting as a frustrated Lewis acid/base pair) for the direct formation of the most stable Re-hydride $[(\mathbf{ReH})(\mathbf{S_1H})\mathbf{L_2}]^{2+}$ (**4**) through $\mathbf{TS_4}$ with an overall free-energy barrier of 18.1 kcal/mol. In addition to heterolytic splitting, homolytic H_2 splitting on Re is predicted to be higher in energy, wherein the H−H bond in **7″** could be split by Re, producing a much more unstable dihydride species that quickly evolves to $[(\mathbf{ReH})(\mathbf{S_1H})\mathbf{L_2}]^{2+}$ (**4**) via intramolecular proton transfer (Scheme S1). This situation also holds true for the H_2 splitting pathways for the formation of the metal and ligand-based adducts $[(\mathbf{ReH})(\mathbf{S_3H})\mathbf{L_2}]^{2+}$ (**6**) and $[(\mathbf{ReH})(\mathbf{S_2H})\mathbf{L_2}]^{2+}$ (**5**) (Figure 3).

The DFT calculations reveal that H_2 binding to Re is uphill in Gibbs free energies, as reflected by the respective relative free energies of 20.9, 25.8, and 14.2 kcal/mol for the formed Re-dihydrogen complexes (**7**, **7′**, and **7″**). This unfavorable preequilibrium of H_2 binding is the main contribution to the barriers for both the heterolytic and homolytic H_2 splitting pathways. This finding is similar to the low H_2 binding affinity of Ni in $[\mathrm{Ni}(\mathrm{P^{Cy}}_2\mathrm{N^{Me}}_2)_2]^{2+}$ reported recently.[6a,e,p] The overall free-energy barriers for the Re system indicate that the heterolytic and homolytic H_2 splitting pathways are energetically comparable with differences of less than 1 kcal/mol. This situation is quite different from the H_2 splitting by $[\mathrm{Ni}(\mathrm{P^{Cy}}_2\mathrm{N^{Me}}_2)_2]^{2+}$, where the heterolytic H_2 splitting pathway is significantly favored over the homolytic one.[6a,e,p] Here, because Re can support higher formal oxidation states and S can donate electrons from its lone pair(s), homolytic cleavage is still viable.

As shown in Figure 3, the ligand-centered adducts $[\mathbf{Re(S_2H)(S_3H)L_2}]^{2+}$ (**1**) and $[\mathbf{Re(S_1H)(S_2H)L_2}]^{2+}$ (**2**) can be formed via direct addition of $\mathbf{H_2}$ to $[\mathbf{ReL_3}]^{2+}$, by overcoming the free energies of activation of 20.0 and 31.6 kcal/mol, respectively. The differential reaction barriers between these two pathways may be explained by the

https://dx.doi.org/10.1021/acscatal.9b04579
ACS Catal. 2020, 10, 3778−3789

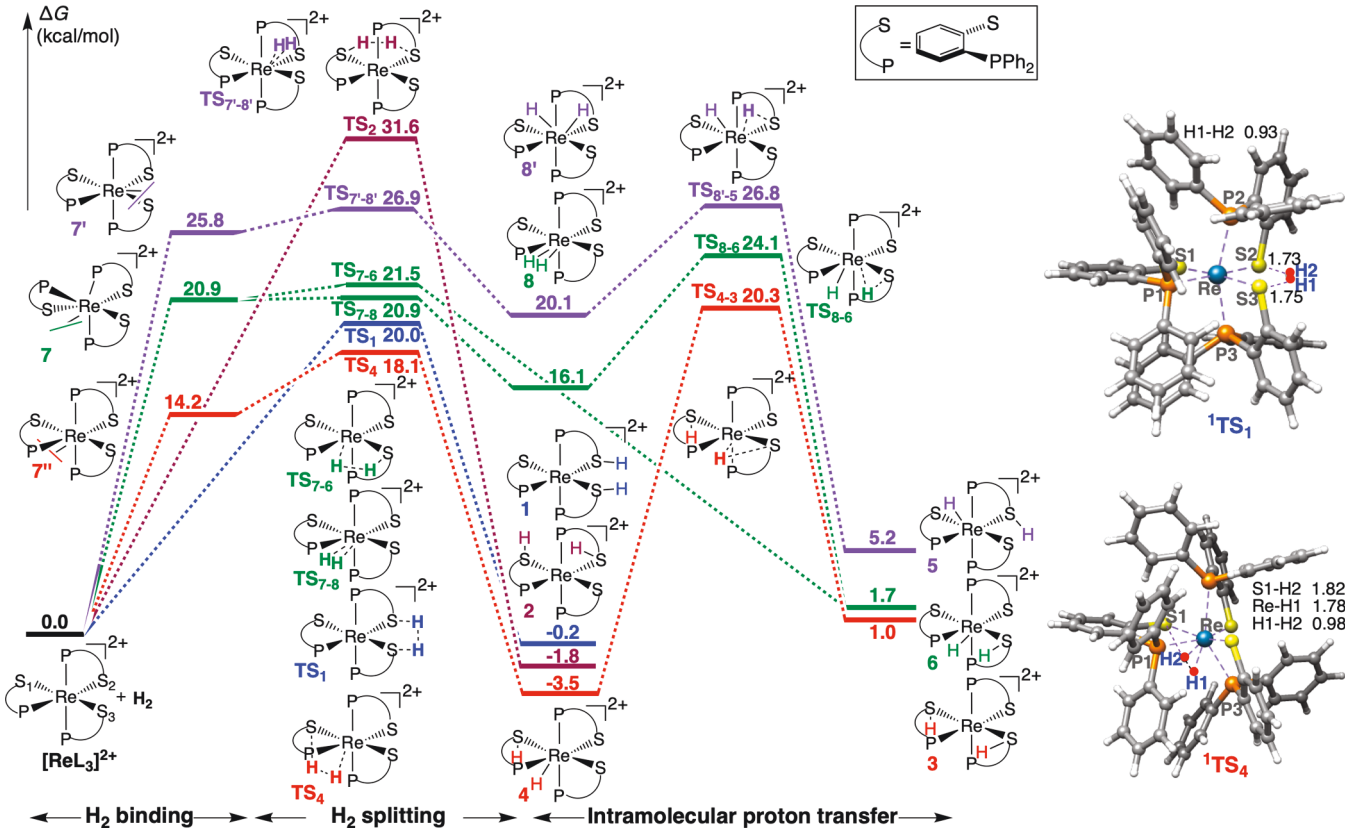

Figure 3. B3PW91-calculated free energy profile for H_2 addition to $[\mathbf{ReL_3}]^{2+}$ to form the intermediate $[\mathbf{ReL_3{\cdot}H_2}]^{2+}$ as depicted in Scheme 2. See Figure S3 for the M06-calculated results.

molecular orbital symmetry. The $\mathbf{TS_1}$ for the formation of **1** is allowed by orbital symmetry, wherein the coplanar S2/S3 sulfur-pair based π^*_{xz} orbital has a good symmetry match with the highest occupied molecular orbital (HOMO) of the approaching $\mathbf{H_2}$. In contrast, the H_2 addition reaction for the formation of **2** is symmetry-forbidden because the S1-p_y orbital is orthogonal to the S2-p_z orbital. Although the twisting renders the reaction symmetry-allowed, this additional distortion costs energy. Another ligand-based product $[\mathbf{Re(S_1H)(S_3H)L_2}]^{2+}$ (**3**) could be formed via intramolecular proton transfer of H from Re in **4** to S3 with a free-energy barrier of 23.8 kcal/mol.

Considering their high relative free energies, the metal dihydrogen (**7** and **7′**) and dihydride (**8** and **8′**) complexes can be ruled out as candidates for the H_2 addition complex. Likewise, rather high barriers for the formation of **2**, **3**, **5**, and **6** make these unlikely candidates. By comparison, the pathway for the formation of the Re-hydride/monothiol **4** is thermodynamically and kinetically most favorable. DFT calculations indicate that the formation **4** is favored over the Re-dithiol **1** in free energy by 1.9 kcal/mol for the truncated ligand model and by 3.3 kcal/mol for the full ligand model (Figure 3). However, the CCSD(T) calculations for the truncated ligand model slightly favor **1** over **4** by 1.3 kcal/mol. Thus, $[\mathbf{(ReH)(S_1H)L_2}]^{2+}$ (**4**) and $[\mathbf{Re(S_2H)(S_3H)L}]^{2+}$ (**1**) may be in equilibrium as H_2 addition complexes. As the rate-determining barrier to the overall mechanism of H_2 oxidation, the calculated barrier of 18.1 kcal/mol ($\mathbf{TS_4}$) for the most favorable heterolytic H_2 bond cleavage is in a good agreement with the free energy of activation calculated from the rate constant (16.5−16.8 kcal/mol, using the Eyring-Polanyi equation). This barrier, computed at the B3PW91 level, has less than 2 kcal/mol deviations from experiment. Although the M06 functional provides similar energetic trends, it predicts higher free energies by about 5 kcal/mol (Figure S3).

Other alternative unfavorable singlet-state pathways for the formation of other H_2 addition isomers and triplet-state pathways toward H_2 oxidation by $[\mathbf{ReL_3}]^{2+}$ were also examined with both B3PW91 and M06 functionals (Schemes S1−S2). All the optimized structures of transition states and intermediates at the B3PW91 and M06 levels are displayed in Figures S4−S9 and Figures S10−S16, respectively.

Theoretical Characterizations of $[\mathbf{ReL_3{\cdot}H}]^+$. The monoprotonated species $[\mathbf{ReL_3{\cdot}H}]^+$, which is believed to be formed via deprotonation of the H_2 addition product by base, has been synthesized by another route and structurally characterized via X-ray crystallography.[12] Computation of all the possible protonation sites (S1, S2, S3, and Re) produced results inconsistent with the experimentally assigned $[\mathbf{Re(S_3H)L_2}]^+$ isomer, for which the H atom bonded to S3 was located in the difference map.[12] However, refinement of this position required constraints. Comparisons of the relative stabilities of both the singlet and triplet states reveal that for the singlet $[\mathbf{Re(S_1H)L_2}]^+$ (**9**), the isomer protonated at S1 is more stable than the other conformers protonated at S2, S3 (Figure 4), and Re (Figure S17). Specifically, the S1-protonated singlet **9** is more stable than the S3-protonated **11′**, which was optimized based on the crystal structure, by 9.4 (singlet) and 7.9 (triplet) kcal/mol, respectively. Like the DFT calculations, CCSD(T) calculations of the truncated models (Figure S2 and Table S11) predict that $[\mathbf{Re(S_1H)L'_2}]^+$ (truncated model for **9**) has the lowest energy and has lower

https://dx.doi.org/10.1021/acscatal.9b04579
ACS Catal. 2020, 10, 3778−3789

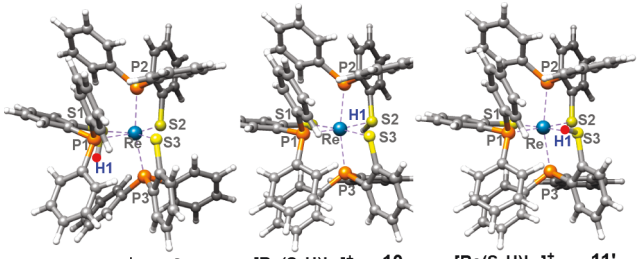

	$[Re(S_1H)L_2]^+$	9	$[Re(S_2H)L_2]^+$	10	$[Re(S_3H)L_2]^+$	11′
Exp.	$^{1,3}\Delta G$	0.0/16.4	$^{1,3}\Delta G$	5.7/2.9	$^{1,3}\Delta G$	9.4/7.9
2.36	Re-S1	**2.53/2.52**	Re-S1	**2.35/2.38**	Re-S1	**2.33/2.34**
2.29	Re-S2	**2.32/2.42**	Re-S2	**2.51/2.49**	Re-S2	**2.32/2.39**
2.29	Re-S3	**2.28/2.39**	Re-S3	**2.31/2.39**	Re-S3	**2.44/2.52**
2.50	Re-P1	**2.55/2.47**	Re-P1	**2.41/2.42**	Re-P1	**2.56/2.44**
2.45	Re-P2	**2.45/2.49**	Re-P2	**2.51/2.48**	Re-P2	**2.49/2.47**
2.44	Re-P3	**2.43/2.47**	Re-P3	**2.46/2.47**	Re-P3	**2.44/2.45**
1.08	S1-H1	**1.37/1.37**	S2-H1	**1.36/1.36**	S3-H1	**1.36/1.36**
168.2	S1-Re-S3	**162.2/171.1**	S1-Re-S3	**168.6/176.5**	S1-Re-S3	**158.5/178.1**
162.6	P1-Re-S2	**160.5/164.7**	P1-Re-S2	**170.4/172.4**	P1-Re-S2	**172.6/173.9**
164.5	P2-Re-S3	**165.3/165.3**	P2-Re-S3	**163.0/167.2**	P2-Re-S3	**166.6/165.8**
110.0	S3-Re-S2	**113.7/103.8**	S3-Re-S2	**96.3/93.1**	S3-Re-S2	**96.2/91.0**
	$^{1}\Delta$CCSD(T)	0.0	$^{1,3}\Delta$CCSD(T)	6.9/9.5	$^{1,3}\Delta$CCSD(T)	8.0/14.4

Figure 4. M06-optimized and experimental (Exp.)[12] geometric parameters are given with bond lengths (Å) and angles (deg) for the ligand-monoprotonated conformers $[\mathbf{Re(LH)L_2}]^+$: protonation at ligand S1 (**9**); S2 (**10**); and S3 (**11′**). The DFT free energies and CCSD(T) energies for the singlet and triplet states (in kcal/mol) are relative to the lowest-energy singlet **9** with full ligand and its truncated ligand model $[\mathbf{Re(S_1H)L'_2}]^+$, respectively. The isomers with an alternative S-H direction (**9′**, **10′**, and **11**) are displayed in the SI.

energy than $[\mathbf{Re(S_3H)L'_2}]^+$ (truncated model for **11′**) by 8.4 (singlet) and 14.8 (triplet) kcal/mol, respectively.

The optimized structures in Figure 4 show the geometries of the singlet state complexes $[\mathbf{Re(S_1H)L_2}]^+$ (**9**), $[\mathbf{Re(S_2H)L_2}]^+$ (**10**), and $[\mathbf{Re(S_3H)L_2}]^+$ (**11′**). In each case, the protonated S always has the longest Re−S bond. The crystal structure shows the longest Re−S bond to S1, with the bonds to S2 and S3 shorter by 0.07 and 0.06 Å, respectively. However, the Re−S1 bond in the experimental structure of $[\mathbf{Re(SH)L_2}]^+$ is actually shorter than in the structure of $\mathbf{ReL_3}$. The only Re−S bond with an increased distance upon protonation is S3. Overall, the root-mean-square deviations from crystal structure Re−L bond lengths and selected bond angles obtained from the singlet **9** are 0.07 Å (except for S_1−H distance) and 3°, respectively, while the deviations obtained from the stable triplet **11′** are 0.11 Å (except for S_3−H distance) and 12°, and those from the higher-energy singlet **11′** are 0.07 Å (except for S_3−H distance) and 10°, respectively. As expected, the calculated S−H distances in all the conformers are near 1.36 Å, a value about 0.3 Å longer than the experimental value.

Based on the above analysis of the calculated relative energies and geometric parameters, and the inability to conclusively locate the H atom experimentally, we proceeded based on the computational result that deprotonation of the H_2 addition product produces the monoprotonated complex $[\mathbf{Re(LH)L_2}]^+$ with the proton on S1. This result is in good accord with the calculated assignment of **4**, $[\mathbf{(ReH)(S_1H)L_2}]^{2+}$, as the main H_2 addition complex. Further deprotonation of the $[\mathbf{Re(S_1H)L_2}]^+$ closes the catalytic cycle of H_2 oxidation to regenerate $[\mathbf{ReL_3}]$ (blue arrows in Scheme 3).

H_2 Evolution Mechanisms. To probe the possible HER mechanisms, the calculated reduction potentials (vs Fc^+/Fc), relative free energies (ΔG), absolute pK_a values, relative pK_a values (vs acetic acid in DCM), and activation barriers ($\Delta G^{\ddagger}$) are used to determine if a calculated structure is acceptable or not. Scheme 3 presents our proposed mechanisms for H_2 production. We focus on the mechanism with the relatively weak acetic acid as used in the experimental CV. According to the experiment, a solution of $[\mathbf{ReL_3}]$ and acetic acid evolves H_2 at −1.7 V and reaches saturation at a molar ratio of 1000-fold excess acid.[12]

In the presence of acetic acid, direct protonation of $[\mathbf{ReL_3}]$ at either ligand (S1, S2, or S3) or the Re center to form the monoprotonated cation $[\mathbf{ReL_3{\cdot}H}]^+$ is predicted to be thermodynamically unfavorable on the basis of very low ΔpK_a values of −39.0 to −25.5 (see details in Table S15). We also calculated the ΔpK_a values of $[\mathbf{ReL_3{\cdot}H}]^+$ with respect to sulfuric and triflic acids, which were used in the other experiments.[12] The DFT calculations indicate that protonation of $[\mathbf{ReL_3}]$ to form $[\mathbf{ReL_3{\cdot}H}]^+$ is thermodynamically unfavorable in the presence of sulfuric acid (ΔpK_a (**9**) = −3.8) but favorable in the presence of triflic acid (ΔpK_a values of 1.0 for **9** Table S16). This prediction is in accord with the experimental preparation of the $[\mathbf{ReL_3{\cdot}H}]^+$ species as the triflate salt.[12] Given the quite low ΔpK_a (vs CH_3COOH) values of $[\mathbf{ReL_3{\cdot}H}]^+$, the pathway in acetic acid must first involve reduction of $[\mathbf{ReL_3}]$ to $[\mathbf{ReL_3}]^-$. As shown in Scheme 3, reduction of $[\mathbf{ReL_3}]$ to $[\mathbf{ReL_3}]^-$, which occurs at a calculated E_1 = −1.45 V, is likely to occur, which is consistent with the experimentally measured value −1.60 V.[12]

Since the reduction of $[\mathbf{ReL_3}]^-$ to $[\mathbf{ReL_3}]^{2-}$ requires a very negative potential, −3.07 V, protonation of $[\mathbf{ReL_3}]^-$ to form the monoprotonated neutral $[\mathbf{ReL_3{\cdot}H}]$ must occur before further reduction. Among all the isomers of $[\mathbf{ReL_3{\cdot}H}]$, the Re-protonated species are thermodynamically favorable over the ligand S-protonated species by about 7 to 9 kcal/mol (Figure S18). For simplicity, we only consider the two most stable Re-protonated species **13** (ΔG = 13.1 kcal/mol) and **13‴** (ΔG = 15.3 kcal/mol). The ΔpK_a values for **13** and **13‴** are calculated to be −9.6 and −11.2, respectively, implying slightly unfavorable thermodynamic process. Thus, excess acid is needed to drive the protonation of $[\mathbf{ReL_3}]^-$, which explains why the observed saturation of current enhancement requires addition of multiple equivalents (>1000 equiv) of acetic acid. Taking into account the modifications including the increase in the acidity from homoconjugation (4.0 units pK_a), the better basis set (2.8 to 4.2 units pK_a), and the 3-fold excess of the acetic acid (3.0 units pK_a) as discussed in the SI, the estimated ΔpK_a (vs acetic acid in DCM) values for **13** and **13‴** are about +0.2 to +1.6 and −1.4 to 0.0, respectively, indicating that protonation of $[\mathbf{ReL_3}]^-$ to form **13** by the acetic acid is likely. The combination of the 3-fold excess of the acid, its increase in acidity from homoconjugation, and the better basis sets will produce a positive ΔpK_a value (see Tables S17−S19 in the SI).

The possibility of an immediate second protonation on $[\mathbf{(ReH)L_3}]$ to form $[\mathbf{ReL_3{\cdot}H_2}]^+$ can be ruled out, by the quite low ΔpK_a = −23.3 for protonation of $[\mathbf{(ReH)L_3}]$ (**13**) to form the most stable isomer $[\mathbf{(ReH)(S_3H)L_2}]^+$ (**25**) (Table S13 and Figure S22). Direct reaction of $[\mathbf{(ReH)L_3}]$ (**13**) with acetic acid to produce H_2 is also thermodynamically unfavorable by 17.6 kcal/mol (Table S20). Therefore, an additional reduction from $[\mathbf{(ReH)L_3}]$ to $[\mathbf{(ReH)L_3}]^-$ is essential. Among all the optimized isomers of $[\mathbf{ReL_3{\cdot}H}]^-$, Re-protonation is thermodynamically much more favorable than the S-protonation by about 7 to 25 kcal/mol (Figure S20). The Re-protonated species **17**, which closely resembles **13**, is most stable within the isomers of $[\mathbf{ReL_3{\cdot}H}]^-$. The calculated reduction potentials for this process, −1.23 V (**13**/**17**) or −1.54 V (**13‴**/**17‴**), are close to the experimentally observed value of −1.70 V.[12] This

https://dx.doi.org/10.1021/acscatal.9b04579
ACS Catal. 2020, 10, 3778−3789

Scheme 3. Proposed Mechanisms for H_2 Oxidation (blue) and H_2 Production (red) with $[ReL_3]$[a]

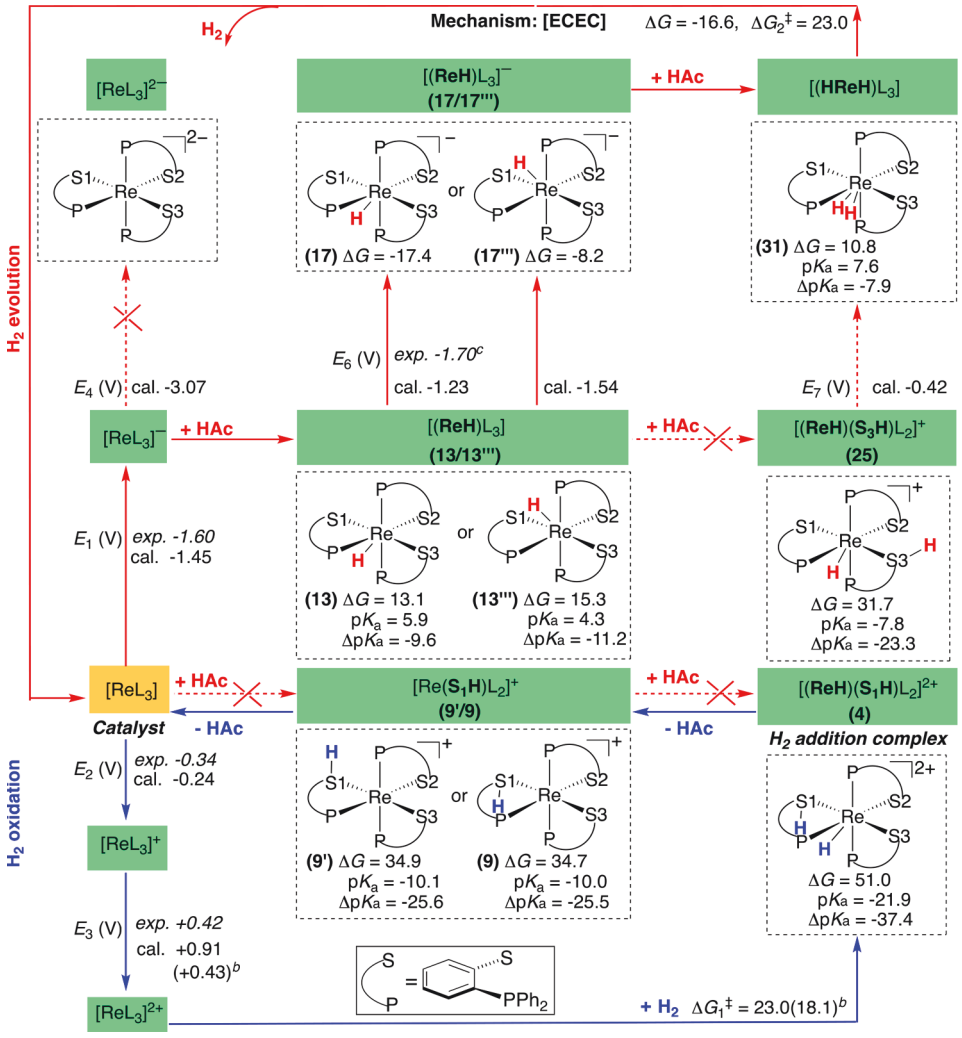

[a]Potentials E (vs $Fc^{+/0}$ in V), relative ΔpK_a (vs HAc), absolute $pK_a(CatH) = \Delta pK_a + pK_a(HAc)$, $pK_a(HAc) = 15.5$ in 1,2-dichloroethane (DCE),[35] relative free energies (ΔG, in kcal/mol, see equations in Scheme S3), and barriers ($\Delta G^{\ddagger}$, in kcal/mol) are given at the M06 level. [b]The values in parentheses are given at the B3PW91 level. All the values of the $[\mathbf{ReL_3}]$ versus acetic acid concentration at a molar ratio of 1:1. [c]The difference may be from experimentally assigning reduction to the peak position, while the calculated value is for the reversible reduction. All the optimized geometries of conformers for $[\mathbf{ReL_3{\cdot}H}]$, $[\mathbf{ReL_3{\cdot}H}]^-$, $[\mathbf{ReL_3{\cdot}H_2}]^+$, and $[\mathbf{ReL_3{\cdot}H_2}]$ are displayed in Figures S18, S20, S22, and S23, respectively. The potential energy surfaces for the protonation of $[\mathbf{ReL_3}]^-$ and **17** by the acetic acid are displayed in Figures S24 and S25, respectively.

result is in contrast with the previous assignment of this reduction being due to the doubly protonated $[\mathbf{ReL_3{\cdot}H_2}]^{+/0}$ potential.[12] As described above the acetic acid is not strong enough to produce doubly protonated $[\mathbf{ReL_3{\cdot}H_2}]^+$. The DFT calculations show that the most stable isomeric couple among all the $[\mathbf{ReL_3{\cdot}H_2}]^{+/0}$ species, $(\mathbf{ReH})(\mathbf{S_3H})\mathbf{L_2}]^{+/0}$ (**25**/**30**), has a much more positive potential (cal. −0.42 V), so under much stronger acid this reduction would occur at a much more positive potential (see Table S21 for reduction potentials E_7 of the other $[\mathbf{ReL_3{\cdot}H_2}]^{+/0}$ couples). Based on the above analysis, we suggested a reassignment of the experimentally observed reduction at −1.70 V to the singly protonated $[\mathbf{ReL_3{\cdot}H}]^{0/-}$ rather than the doubly protonated $[\mathbf{ReL_3{\cdot}H_2}]^{+/0}$.

Upon addition of the second proton to $[(\mathbf{ReH})\mathbf{L_3}]^-$, direct proton delivery to the Re in $[(\mathbf{ReH})\mathbf{L_3}]^-$ (**17**) to form the Re-dihydride species $[(\mathbf{HReH})\mathbf{L_3}]$ (**31**) is thermodynamically more favorable ($\Delta pK_a = -7.9$, Scheme 3) as compared to proton delivery to the S to form the most stable Re-hydride/monothiol $[(\mathbf{ReH})(\mathbf{S_3H})\mathbf{L_2}]$ (**30**/**30a**, differing by H orientation) among all the doubly protonated neutral $[\mathbf{ReL_3{\cdot}H_2}]$ ($\Delta pK_a = -9.2$ and -10.5, Table S14 and Figure S23). Considering the modifications including the increase in the acidity from homoconjugation, the better basis set, and the 3-fold excess of the acetic acid as discussed in the SI, the evaluated ΔpK_a (vs acetic acid in DCM) value for **31** is +1.9 ∼ +3.3, suggesting that protonation of **17** to form **31** by the acetic acid can occur. The following homolytic reductive elimination of H_2 from this Re-dihydride species (**31**) is thermodynamically favorable by 16.6 kcal/mol through a barrier of 23.0 kcal/mol relative to **31** (Figure S25). As shown in Figure 5, the calculated transition state for the H_2 release involves both the H−H formation (H−H distance of 0.77 Å in $\mathbf{TS_{H2}}$ vs 1.78 Å in **31**) and the H_2 release (Re−H distances of 2.31 and 2.28 Å in $\mathbf{TS_{H2}}$ vs 1.66 and 1.65 Å in **31**). The predicted catalytic cycle is an [ECEC] mechanism, in which the active species for H_2 evolution is a Re-dihydride instead of a Re-dithiol as proposed earlier.[12]

https://dx.doi.org/10.1021/acscatal.9b04579
ACS Catal. 2020, 10, 3778−3789

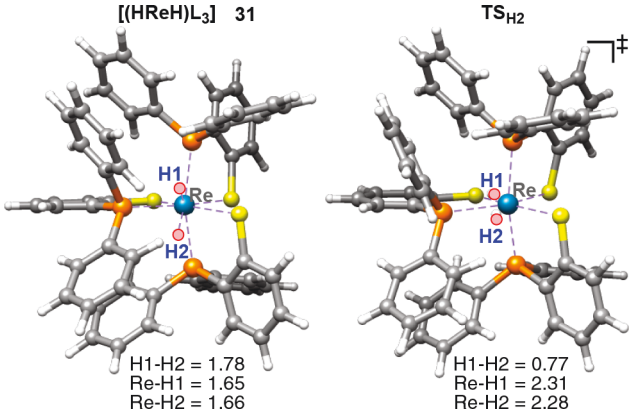

Figure 5. M06-optimized structures of the Re-dihydride intermediate (**31**) and the transition state for the H_2 release from **31** ($\mathbf{TS_{H2}}$). All the key bond lengths are given in Å.

Comparisons of the calculated barriers among the protonation of $[\mathbf{ReL_3}]^-$ (Figure S24) and **17** (Figure S25) by the acetic acid and H_2 release (Figure S25) as discussed in the SI reveal that the homolytic reductive elimination of H_2 from the Re-dihydride species (**31**) is in better agreement with the rate-determining step in the experiment, which shows a large kinetic isotope effect (KIE of 9 ± 1) and a second order dependence on $[H^+]$ with a similar rate constant for either acetic or sulfuric acid.[12]

4. CONCLUSION

In summary, DFT and high-level *ab initio* methods including CCSD(T) and CASSCF in combination with experimental work[12] were used to investigate the electrocatalytic H_2 oxidation and H_2 evolution catalyzed by rhenium-tri(thiolate) complexes $[\mathbf{ReL_3}]$ (L = DPPBT = diphenylphosphinobenzenethiolate, a noninnocent ligand).

Based on comparisons of thermodynamic and kinetic predictions with the experimental data, DFT calculations predict that the H_2 oxidation reaction (HOR) proceeds by an EECC mechanism, in which stepwise oxidization of $[\mathbf{ReL_3}]$ by two electrons to form $[\mathbf{ReL_3}]^{2+}$ is followed by the H_2 addition to form the thermodynamically and kinetically favorable Re-hydride/monothiol $[\mathbf{(ReH)(S_1H)L_2}]^{2+}$ or Re-dithiols $[\mathbf{Re(S_2H)(S_3H)L}]^{2+}$, and then by successive deprotonations to regenerate $[\mathbf{ReL_3}]$ via $[\mathbf{Re(S_1H)L_2}]^+$.

The H_2 evolution reaction (HER) in excess weak (acetic) acid is an ECEC mechanism that begins with the reduction of $[\mathbf{ReL_3}]$ to $[\mathbf{ReL_3}]^-$, followed by protonation at Re to produce $[\mathbf{(ReH)L_3}]$, which undergoes another reduction to $[\mathbf{(ReH)L_3}]^-$. Delivery of the final proton to the Re in $[\mathbf{(ReH)L_3}]^-$ forms the Re-dihydride species $[\mathbf{(HReH)L_3}]$. Production of H_2 occurs via reductive elimination through a Re-H_2 adduct.

The mechanistic analysis indicates that the HOR thermodynamically and kinetically favors a Re-hydride/monothiol intermediate, while the HER favors Re-dihydride intermediates, in contrast to the Re-dithiols that were proposed earlier.[12] The structurally characterized species $[\mathbf{Re(LH)L_2}]^+$ is likely part of the HOR catalytic cycle but not part of the HER catalytic cycle in a weak acid such as acetic but could be involved in this cycle with stronger acid. Although the previous computational study[12b] used the suitable M06 functional, they considered only the S3 site, missing the other active sites for H_2 addition, protonation, in a variety of redox states for the various species occurring in the proposed mechanisms for H_2 oxidation and H_2 production. The major improvement in the present computations compared with the previous mechanistic study[12b] is that we examined all the possible sites on any of the S ligands (S1, S2, and S3) and Re.

DFT redox potential calculations suggested a reassignment of the experimentally observed peak −1.70 V to the singly protonated $[\mathbf{ReL_3{\cdot}H}]^{0/-}$ couple rather than the doubly protonated $[\mathbf{ReL_3{\cdot}H_2}]^{+/0}$ couple, as acetic acid is too weak to form this more easily reduced species.

The detailed mechanisms using these rhenium-tris(thiolate) complexes are very helpful for rationally designing the effective HOR and HER electrocatalysts.

■ ASSOCIATED CONTENT

Supporting Information

The Supporting Information is available free of charge at https://pubs.acs.org/doi/10.1021/acscatal.9b04579.

> Benchmarking of different DFT functionals for relative free energies, geometric structures optimized in gas phase and solution, and redox potentials. Relative free energies and geometric structures of truncated models. All the pathways, optimized geometries of intermediates, and transition states for H_2 oxidation with $[\mathbf{ReL_3}]^{2+}$ at both M06 and B3PW91 levels. M06-optimized structures and relative free energies of isomers for $[\mathbf{(ReH)L_3}]^+$, $[\mathbf{ReL_3{\cdot}H_2}]^+$, and $[\mathbf{ReL_3{\cdot}H_2}]$. M06-optimized geometries of intermediates and transition states of $[\mathbf{ReL_3{\cdot}H}]^{0/-}$. Calculated redox potentials and pK_a values. Relative free energies for reaction of $[\mathbf{ReL_3{\cdot}H}]^{+/0/-}$ with acetic acid. Analysis of the modifications in the ΔpK_a calculations. The potential energy surfaces for the protonation of $[\mathbf{ReL_3}]^-$ and **17** by the acetic acid. CCSD(T) single-point energies of some isomers of $[\mathbf{ReL_3{\cdot}H_2}]^{+/0}$. CASSCF results on the active spaces, all the configurations, coefficients, and electron occupancy numbers. Cartesian coordinates and absolute energies. (PDF)

■ AUTHOR INFORMATION

Corresponding Authors

Craig A. Grapperhaus − *Department of Chemistry, University of Louisville, Louisville, Kentucky 40292, United States;* orcid.org/0000-0003-4889-2645; Email: grapperhaus@louisville.edu

Michael B. Hall − *Department of Chemistry, Texas A&M University, College Station, Texas 77845, United States;* orcid.org/0000-0003-3263-3219; Email: mbhall@tamu.edu

Authors

Hao Tang − *Department of Chemistry, Texas A&M University, College Station, Texas 77845, United States;* orcid.org/0000-0003-0323-0349

Edward N. Brothers − *Science Program, Texas A&M University at Qatar, Doha, Qatar*

Complete contact information is available at: https://pubs.acs.org/10.1021/acscatal.9b04579

Author Contributions

All authors have given approval to the final version of the manuscript.

https://dx.doi.org/10.1021/acscatal.9b04579
ACS Catal. 2020, 10, 3778−3789

Notes

The authors declare no competing financial interest.

■ ACKNOWLEDGMENTS

We acknowledge financial support from the Qatar National Research Fund under NPRP, Grant No. 05-318-1-063 (for support of the preliminary results for this project), The Welch Foundation, Grant A-0648, and the National Science Foundation, Grant CHE-1664866. Computer time was provided by the TAMU Supercomputer Facility, and software was provided by the Laboratory for Molecular Simulation.

■ REFERENCES

(1) (a) McEvoy, J. P.; Brudvig, G. W. Water-Splitting Chemistry of Photosystem II. *Chem. Rev.* **2006**, *106*, 4455−4483. (b) Saveánt, J.-M. Molecular Catalysis of Electrochemical Reactions. Mechanistic Aspects. *Chem. Rev.* **2008**, *108*, 2348−2378. (c) Cook, T. R.; Dogutan, D. K.; Reece, S. Y.; Surendranath, Y.; Teets, T. S.; Nocera, D. G. Solar Energy Supply and Storage for the Legacy and Nonlegacy Worlds. *Chem. Rev.* **2010**, *110*, 6474−6502. (d) Gray, H. B. Powering the Planet with Solar Fuel. *Nat. Chem.* **2009**, *1*, 7. (e) Dalle, K. E.; Warnan, J.; Leung, J. J.; Reuillard, B.; Karmel, I. S.; Reisner, E. Electro- and Solar-Driven Fuel Synthesis with First Row Transition Metal Complexes. *Chem. Rev.* **2019**, *119*, 2752−2875.

(2) (a) Lubitz, W.; Tumas, W. Hydrogen: An Overview. *Chem. Rev.* **2007**, *107*, 3900−3903 and references contained within this special issue. (b) Lewis, N. S.; Nocera, D. G. Powering the planet: Chemical Challenges in Solar Energy Utilization. *Proc. Natl. Acad. Sci. U. S. A.* **2006**, *103*, 15729−15735. (c) Nocera, D. G. Chemistry of Personalized Solar Energy. *Inorg. Chem.* **2009**, *48*, 10001−10017. (d) Esswein, A. J.; Nocera, D. G. Hydrogen Production by Molecular Photocatalysis. *Chem. Rev.* **2007**, *107*, 4022−4047. (e) Denny, J. A.; Darensbourg, M. Y. Metallodithiolates as Ligands in Coordination, Bioinorganic, and Organometallic Chemistry. *Chem. Rev.* **2015**, *115*, 5248−5273. (f) Schilter, D.; Camara, J. M.; Huynh, M. T.; Hammes-Schiffer, S.; Rauchfuss, T. B. Hydrogenase Enzymes and Their Synthetic Models: The Role of Metal Hydrides. *Chem. Rev.* **2016**, *116*, 8693−8749. (g) McKone, J. R.; Marinescu, S. C.; Brunschwig, B. S.; Winkler, J. R.; Gray, H. B. Earth-abundant Hydrogen Evolution Electrocatalysts. *Chem. Sci.* **2014**, *5*, 865−878.

(3) (a) Barton, B. E.; Olsen, M. T.; Rauchfuss, T. B. Artificial Hydrogenases. *Curr. Opin. Biotechnol.* **2010**, *21*, 292−297. (b) Fontecilla-Camps, J. C.; Volbeda, A.; Cavazza, C.; Nicolet, Y. Structure/Function Relationships of [NiFe]- and [FeFe]-Hydrogenases. *Chem. Rev.* **2007**, *107*, 4273−4303. (c) Shima, S.; Pilak, O.; Vogt, S.; Schick, M.; Stagni, M. S.; Meyer-Klaucke, W.; Warkentin, E.; Thauer, R. K.; Ermler, U. The Crystal Structure of [Fe]-hydrogenase Reveals the Geometry of the Active Site. *Science* **2008**, *321*, 572−575. (d) Tard, C.; Pickett, C. J. Structural and Functional Analogues of the Active Sites of the [Fe]-, [NiFe]-, and [FeFe]-Hydrogenases. *Chem. Rev.* **2009**, *109*, 2245−2274. (e) Lubitz, W.; Ogata, H.; Rüdiger, O.; ReIjerse, E. Hydrogenases. *Chem. Rev.* **2014**, *114*, 4081−4148. (f) Simmons, T. R.; Berggren, G.; Bacchi, M.; Fontecave, M.; Artero, V. Mimicking Hydrogenases: From Biomimetics to Artificial Enzymes. *Coord. Chem. Rev.* **2014**, *270−271*, 127−150. (g) Chambers, G. M.; Huynh, M. T.; Li, Y.; Hammes-Schiffer, S.; Rauchfuss, T. B. Models of the Ni-L and Ni-SIa States of the [NiFe]-Hydrogenase Active Site. *Inorg. Chem.* **2016**, *55*, 419−431. (h) Greene, B. L.; Vansuch, G. E.; Wu, C.-H.; Adams, M. W. W.; Dyer, R. B. Glutamate Gated Proton-Coupled Electron Transfer Activity of a [NiFe]-Hydrogenase. *J. Am. Chem. Soc.* **2016**, *138*, 13013−13021. (i) Ulloa, O. A.; Huynh, M. T.; Richers, C. P.; Bertke, J. A.; Nilges, M. J.; Hammes-Schiffer, S.; Rauchfuss, T. B. Mechanism of H_2 Production by Models for the [NiFe]-Hydrogenases: Role of Reduced Hydrides. *J. Am. Chem. Soc.* **2016**, *138*, 9234−9245. (j) Hugenbruch, S.; Shafaat, H. S.; Krämer, T.; Delgado-Jaime, M. U.; Weber, K.; Neese, F.; Lubitza, W.; DeBeer, S. In Search of Metal Hydrides: an X-ray Absorption and Emission Study of [NiFe] Hydrogenase Model Complexes. *Phys. Chem. Chem. Phys.* **2016**, *18*, 10688−10699. (k) Qiu, S.; Azofra, L. M.; MacFarlane, D. R.; Sun, C. Unraveling the Role of Ligands in the Hydrogen Evolution Mechanism Catalyzed by [NiFe] Hydrogenases. *ACS Catal.* **2016**, *6*, 5541−5548. (l) Yen, T.-H.; He, Z.-C.; Lee, G.-H.; Tseng, M.-C.; Shen, Y.-H.; Tseng, T.-W.; Liaw, W.-F.; Chiang, M.-H. Reduced Thione Ligation is Preferred over Neutral Phosphine Ligation in Diiron Biomimics regarding Electronic Functionality: a Spectroscopic and Computational Investigation. *Chem. Commun.* **2017**, *53*, 332−335. (m) Sommer, C.; Adamska-Venkatesh, A.; Pawlak, K.; Birrell, J. A.; Rüdiger, O.; Reijerse, E. J.; Lubitz, W. Proton Coupled Electronic Rearrangement within the H-Cluster as an Essential Step in the Catalytic Cycle of [FeFe] Hydrogenases. *J. Am. Chem. Soc.* **2017**, *139*, 1440−1443. (n) Lunsford, A. M.; Goldstein, K. F.; Cohan, M. A.; Denny, J. A.; Bhuvanesh, N.; Ding, S.; Hall, M. B.; Darensbourg, M. Y. Comparisons of MN_2S_2 vs. Bipyridine as Redox-active Ligands to Manganese and Rhenium in $(L{-}L)M'(CO)_3Cl$ Complexes. *Dalton Trans.* **2017**, *46*, 5175−5182. (o) Ding, S.; Ghosh, P.; Lunsford, A. M.; Wang, N.; Bhuvanesh, N.; Hall, M. B.; Darensbourg, M. Y. Hemilabile Bridging Thiolates as Proton Shuttles in Bioinspired H_2 Production Electrocatalysts. *J. Am. Chem. Soc.* **2016**, *138*, 12920−12927. (p) Ghosh, P.; Ding, S.; Chupik, R. B.; Quiroz, M.; Hsieh, C.-H.; Bhuvanesh, N.; Hall, M. B.; Darensbourg, M. Y. A Matrix of Heterobimetallic Complexes for Interrogation of Hydrogen Evolution Reaction Electrocatalysts. *Chem. Sci.* **2017**, *8*, 8291. (q) Ding, S.; Ghosh, P.; Darensbourg, M. Y.; Hall, M. B. Interplay of Hemilability and Redox Activity in Models of Hydrogenase Active Sites. *Proc. Natl. Acad. Sci. U. S. A.* **2017**, *114*, E9775. (r) Tang, H.; Hall, M. B. Biomimetics of [NiFe]-Hydrogenase: Nickel- or Iron-Centered Proton Reduction Catalysis? *J. Am. Chem. Soc.* **2017**, *139*, 18065−18070. (s) Brazzolotto, D.; Wang, L.; Tang, H.; Gennari, M.; Queyriaux, N.; Philouze, C.; Demeshko, S.; Meyer, F.; Orio, M.; Artero, V.; Hall, M. B.; Duboc, C. Tuning Reactivity of Bioinspired [NiFe]-Hydrogenase Models by Ligand Design and Modeling the CO Inhibition Process. *ACS Catal.* **2018**, *8*, 10658−10667. (t) Wiedner, E. S. Thermodynamic Hydricity of [FeFe]-Hydrogenases. *J. Am. Chem. Soc.* **2019**, *141*, 7212−7222. (u) Popescu, C. V.; Ding, S.; Ghosh, P.; Hall, M. B.; Cohara, M. Mössbauer Spectroscopy and Theoretical Studies of Iron Bimetallic Complexes Showing Electrocatalytic Hydrogen Evolution. *Inorg. Chem.* **2019**, *58*, 7069−7077. (v) Yang, X.; Elrod, L.; Reibenspies, J. H.; Hall, M. B.; Darensbourg, M. Y. Oxygen Uptake in Complexes Related to [NiFeS]- and [NiFeSe]-hydrogenase Active Sites. *Chem. Sci.* **2019**, *10*, 1368. (w) Ahmed, M. E.; Chattopadhyay, S.; Wang, L.; Brazzolotto, D.; Pramanik, D.; Aldakov, D.; Fize, J.; Morozan, A.; Gennari, M.; Duboc, C.; Dey, A.; Artero, V. Hydrogen Evolution from Aqueous Solutions Mediated by a Heterogenized [NiFe]-Hydrogenase Model: Low pH Enables Catalysis through an Enzyme-Relevant Mechanism. *Angew. Chem., Int. Ed.* **2018**, *57*, 16001−16004.

(4) (a) Elgrishi, N.; McCarthy, B. D.; Rountree, E. S.; Dempsey, J. L. Reaction Pathways of Hydrogen-Evolving Electrocatalysts: Electrochemical and Spectroscopic Studies of Proton-Coupled Electron Transfer Processes. *ACS Catal.* **2016**, *6*, 3644−3659. (b) Willkomm, J.; Orchard, K. L.; Reynal, A.; Pastor, E.; Durrant, J. R.; Reisner, E. Dye-sensitised Semiconductors Modified with Molecular Catalysts for Light-Driven H_2 Production. *Chem. Soc. Rev.* **2016**, *45*, 9−23. (c) Kandemir, B.; Chakraborty, S.; Guo, Y.; Bren, K. L. Semisynthetic and Biomolecular Hydrogen Evolution Catalysts. *Inorg. Chem.* **2016**, *55*, 467−477. (d) Tran, P. D.; Barber, J. Protonreduction to Hydrogen in Biological and Chemical Systems. *Phys. Chem. Chem. Phys.* **2012**, *14*, 13772−13784. (e) Ginovska-Pangovska, B.; Dutta, A.; Reback, M. L.; Linehan, J. C.; Shaw, W. J. Beyond the Active Site: The Impact of the Outer Coordination Sphere on Electrocatalysts for Hydrogen Production and Oxidation. *Acc. Chem. Res.* **2014**, *47*, 2621−2630. (f) Solis, B. H.; Hammes-Schiffer, S. Proton-Coupled Electron Transfer in Molecular Electrocatalysis: Theoretical Methods and Design Principles. *Inorg. Chem.* **2014**, *53*, 6427−6443. (g) DuBois, D. L. Development of Molecular Electrocatalysts for Energy Storage. *Inorg. Chem.* **2014**, *53*, 3935−3960.

(5) (a) Hu, X.; Cossairt, B. M.; Brunschwig, B. S.; Lewis, N. S.; Peters, J. C. Electrocatalytic Hydrogen Evolution by Cobalt Difluoroboryl-diglyoximate Complexes. *Chem. Commun.* **2005**, 4723−4725. (b) Baffert, C.; Artero, V.; Fontecave, M. Cobaloximes as Functional Models for Hydrogenases. 2. Proton Electroreduction Catalyzed by Difluoroborylbis(dimethylglyoximato)cobalt(II) Complexes in Organic Media. *Inorg. Chem.* **2007**, *46*, 1817−1824. (c) Hu, X.; Brunschwig, B. S.; Peters, J. C. Electrocatalytic Hydrogen Evolution at Low Overpotentials by Cobalt Macrocyclic Glyoxime and Tetraimine Complexes. *J. Am. Chem. Soc.* **2007**, *129*, 8988−8998. (d) Dempsey, J. L.; Brunschwig, B. S.; Winkler, J. R.; Gray, H. B. Hydrogen Evolution Catalyzed by Cobaloximes. *Acc. Chem. Res.* **2009**, *42*, 1995−2004. (e) Jacques, P.-A.; Artero, V.; Pécaut, J.; Fontecave, M. Cobalt and Nickel Diimine-dioxime Complexes as Molecular Electrocatalysts for Hydrogen Evolution with Low Overvoltages. *Proc. Natl. Acad. Sci. U. S. A.* **2009**, *106*, 20627−20632. (f) Dempsey, J. L.; Winkler, J. R.; Gray, H. B. Kinetics of Electron Transfer Reactions of H_2-Evolving Cobalt Diglyoxime Catalysts. *J. Am. Chem. Soc.* **2010**, *132*, 1060−1065. (g) Berben, L. A.; Peters, J. C. Hydrogen Evolution by Cobalt Tetraiminecatalysts Adsorbed on Electrode Surfaces. *Chem. Commun.* **2010**, *46*, 398−400. (h) Muckerman, J. T.; Fujita, E. Theoretical Studies of the Mechanism of Catalytic Hydrogen Production by a Cobaloxime. *Chem. Commun.* **2011**, *47*, 12456−12458. (i) Solis, B. H.; Hammes-Schiffer, S. Theoretical Analysis of Mechanistic Pathways for Hydrogen Evolution Catalyzed by Cobaloximes. *Inorg. Chem.* **2011**, *50*, 11252−11262. (j) Solis, B. H.; Hammes-Schiffer, S. Substituent Effects on Cobalt Diglyoxime Catalysts for Hydrogen Evolution. *J. Am. Chem. Soc.* **2011**, *133*, 19036−19039. (k) Solis, B. H.; Yu, Y.; Hammes-Schiffer, S. Effects of Ligand Modification and Protonation on Metal Oxime Hydrogen Evolution Electrocatalysts. *Inorg. Chem.* **2013**, *52*, 6994−6999. (l) Wakerley, D. W.; Reisner, E. Development and Understanding of Cobaloxime Activity through Electrochemical Molecular Catalyst Screening. *Phys. Chem. Chem. Phys.* **2014**, *16*, 5739−5746. (m) Kaeffer, N.; Chavarot-Kerlidou, M.; Artero, V. Hydrogen Evolution Catalyzed by Cobalt Diimine−Dioxime Complexes. *Acc. Chem. Res.* **2015**, *48*, 1286−1295. (n) Rountree, E. S.; Martin, D. J.; McCarthy, B. D.; Dempsey, J. L. Linear Free Energy Relationships in the Hydrogen Evolution Reaction: Kinetic Analysis of a Cobaloxime Catalyst. *ACS Catal.* **2016**, *6*, 3326−3335. (o) Lacy, D. C.; Roberts, G. M.; Peters, J. C. The Cobalt Hydride that Never Was: Revisiting Schrauzer's "Hydridocobaloxime. *J. Am. Chem. Soc.* **2015**, *137*, 4860−4864. (p) Estes, D. P.; Grills, D. C.; Norton, J. R. The Reaction of Cobaloximes with Hydrogen: Products and Thermodynamics. *J. Am. Chem. Soc.* **2014**, *136*, 17362−17365. (q) Khandelwal, S.; Zamader, A.; Nagayach, V.; Dolui, D.; Mir, A. Q.; Dutta, A. Inclusion of Peripheral Basic Groups Activates Dormant Cobalt-Based Molecular Complexes for Catalytic H_2 Evolution in Water. *ACS Catal.* **2019**, *9*, 2334−2344. (r) Chu, X.; Jin, J.; Ming, B.; Pang, M.; Yu, X.; Tung, C.; Wang, W. Bimetallic Nickel−Cobalt Hydrides in H_2 Activation and Catalytic Proton Reduction. *Chem. Sci.* **2019**, *10*, 761.

(6) (a) Helm, M. L.; Stewart, M. P.; Bullock, R. M.; DuBois, M. R.; DuBois, D. L. A Synthetic Nickel Electrocatalyst with a Turnover Frequency above 100,000 s^{-1} for H_2 Production. *Science* **2011**, *333*, 863−866. (b) O'Hagan, M.; Shaw, W. J.; Raugei, S.; Chen, S.; Yang, J. Y.; Kilgore, U. J.; DuBois, D. L.; Bullock, R. M. Moving Protons with Pendant Amines: Proton Mobility in a Nickel Catalyst for Oxidation of Hydrogen. *J. Am. Chem. Soc.* **2011**, *133*, 14301−14312. (c) Horvath, S.; Fernandez, L. E.; Soudackov, A. V.; Hammes-Schiffer, S. Insights into Proton-coupled Electron Transfer Mechanisms of Electrocatalytic H_2 Oxidation and Production. *Proc. Natl. Acad. Sci. U. S. A.* **2012**, *109*, 15663−15668. (d) Raugei, S.; Chen, S.; Ho, M.-H.; Ginovska-Pangovska, B.; Rousseau, R. J.; Dupuis, M.; DuBois, D. L.; Bullock, R. M. The Role of Pendant Amines in the Breaking and Forming of Molecular Hydrogen Catalyzed by Nickel Complexes. *Chem. - Eur. J.* **2012**, *18*, 6493−6506. (e) Wiese, S.; Kilgore, U. J.; Ho, M.-H.; Raugei, S.; DuBois, D. L.; Bullock, R. M.; Helm, M. L. Hydrogen Production Using Nickel Electrocatalysts with Pendant Amines: Ligand Effects on Rates and Overpotentials. *ACS Catal.* **2013**, *3*, 2527−2535. (f) Stewart, M. P.; Ho, M.-H.; Wiese, S.; Lindstrom, M. L.; Thogerson, C. E.; Raugei, S.; Bullock, R. M.; Helm, M. L. High Catalytic Rates for Hydrogen Production Using Nickel Electrocatalysts with Seven-Membered Cyclic Diphosphine Ligands Containing One Pendant Amine. *J. Am. Chem. Soc.* **2013**, *135*, 6033−6046. (g) Chen, S.; Ho, M.-H.; Bullock, R. M.; DuBois, D. L.; Dupuis, M.; Rousseau, R.; Raugei, S. Computing Free Energy Landscapes: Application to Ni-based Electrocatalysts with Pendant Amines for H_2 Production and Oxidation. *ACS Catal.* **2014**, *4*, 229−242. (h) Appel, A. M.; Pool, D. H.; O'Hagan, M.; Shaw, W. J.; Yang, J. Y.; Rakowski Dubois, M.; Dubois, D. L.; Bullock, R. M. $[Ni(PPh2NBn_2)_2(CH_3CN)]^{2+}$ as an Electrocatalyst for H_2 Production: Dependence on Acid Strength and Isomer Distribution. *ACS Catal.* **2011**, *1*, 777−785. (i) Wiedner, E. S.; Brown, H. J. S.; Helm, M. L. Kinetic Analysis of Competitive Electrocatalytic Pathways: New Insights into Hydrogen Production with Nickel Electrocatalysts. *J. Am. Chem. Soc.* **2016**, *138*, 604−616. (j) Rountree, E. S.; Dempsey, J. L. Potential-Dependent Electrocatalytic Pathways: Controlling Reactivity with pKa for Mechanistic Investigation of a Nickel-Based Hydrogen Evolution Catalyst. *J. Am. Chem. Soc.* **2015**, *137*, 13371−13380. (k) Han, Z.; Shen, L.; Brennessel, W. W.; Holland, P. L.; Eisenberg, R. Nickel Pyridinethiolate Complexes as Catalysts for the Light-Driven Production of Hydrogen from Aqueous Solutions in Noble-Metal-Free Systems. *J. Am. Chem. Soc.* **2013**, *135*, 14659−14669. (l) Solis, B. H.; Maher, A. G.; Dogutan, D. K.; Nocera, D. G.; Hammes-Schiffer, S. Nickel Phlorin Intermediate Formed by Proton-coupled Electron Transfer in Hydrogen Evolution Mechanism. *Proc. Natl. Acad. Sci. U. S. A.* **2016**, *113*, 485−492. (m) Rountree, E. S.; Dempsey, J. L. Reactivity of Proton Sources with a Nickel Hydride Complex in Acetonitrile: Implications for the Study of Fuel-Forming Catalysts. *Inorg. Chem.* **2016**, *25*, 5079−5087. (n) Raugei, S.; Helm, M. L.; Hammes-Schiffer, S.; Appel, A. M.; O'Hagan, M.; Wiedner, E. S.; Bullock, R. M. Experimental and Computational Mechanistic Studies Guiding the Rational Design of Molecular Electrocatalysts for Production and Oxidation of Hydrogen. *Inorg. Chem.* **2016**, *55*, 445−460. (o) Das, A. K.; Engelhard, M. H.; Bullock, R. M.; Roberts, J. A. S. A Hydrogen−Evolving $Ni(P_2N_2)_2$ Electrocatalyst Covalently Attached to a Glassy Carbon Electrode: Preparation, Characterization, and Catalysis. Comparisons with the Homogeneous Analogue. *Inorg. Chem.* **2014**, *53*, 6875−6885. (p) Horvath, S.; Fernandez, L. E.; Appel, A. M.; Hammes-Schiffer, S. pH-Dependent Reduction Potentials and Proton-Coupled Electron Transfer Mechanisms in Hydrogen-Producing Nickel Molecular Electrocatalysts. *Inorg. Chem.* **2013**, *52*, 3643−3652. (q) Raugei, S.; DuBois, D. L.; Rousseau, R.; Chen, S.; Ho, M.-H.; Bullock, R. M.; Dupuis, M. Toward Molecular Catalysts by Computer. *Acc. Chem. Res.* **2015**, *48*, 248−255. (r) Jain, R.; Mamun, A. A.; Buchanan, R. M.; Kozlowski, P. M.; Grapperhaus, C. A. Ligand-Assisted Metal-Centered Electrocatalytic Hydrogen Evolution upon Reduction of a Bis(thiosemicarbazonato)Ni(II) Complex. *Inorg. Chem.* **2018**, *57*, 13486−13493. (s) Klug, C. M.; Carfenas, A. J. P.; Bullock, R. M.; O'Hagan, M.; Wiedner, E. S. Reversing the Tradeoff between Rate and Overpotential in Molecular Electrocatalysts for H_2 Production. *ACS Catal.* **2018**, *8*, 3286−3296. (t) Slater, J. W.; Marguet, S. C.; Monaco, H. A.; Shafaat, H. S. Going beyond Structure: Nickel-Substituted Rubredoxin as a Mechanistic Model for the [NiFe] Hydrogenases. *J. Am. Chem. Soc.* **2018**, *140*, 10250−10262. (u) Maher, A. G.; Liu, M.; Nocera, D. G. Ligand Noninnocence in Nickel Porphyrins: Nickel Isobacteriochlorin Formation under Hydrogen Evolution Conditions. *Inorg. Chem.* **2019**, *58*, 7958−7968.

(7) (a) Kaur-Ghumaan, S.; Schwartz, L.; Lomoth, R.; Stein, M.; Ott, S. Catalytic Hydrogen Evolution from Mononuclear Iron(II) Carbonyl Complexes as Minimal Functional Models of the [FeFe] Hydrogenase Active Site. *Angew. Chem., Int. Ed.* **2010**, *49*, 8033−8036. (b) Royer, A. M.; Salomone-Stagni, M.; Rauchfuss, T. B.; Meyer- Klaucke, W. Iron Acyl Thiolato Carbonyls: Structural Models for the Active Site of the [Fe]−Hydrogenase (Hmd). *J. Am. Chem. Soc.* **2010**, *132*, 16997−17003. (c) Rose, M. J.; Gray, H. B.; Winkler, J. R. Hydrogen Generation Catalyzed by Fluorinated Diglyoxime−Iron

https://dx.doi.org/10.1021/acscatal.9b04579
ACS Catal. 2020, 10, 3778−3789

Complexes at Low Overpotentials. *J. Am. Chem. Soc.* **2012**, *134*, 8310−8313. (d) Harshan, A. K.; Solis, B. H.; Winkler, J. R.; Gray, H. B.; Hammes-Schiffer, S. Computational Study of Fluorinated Diglyoxime-Iron Complexes: Tuning the Electrocatalytic Pathways for Hydrogen Evolution. *Inorg. Chem.* **2016**, *55*, 2934−2940. (e) Bethel, R. D.; Crouthers, D. J.; Hsieh, C.-H.; Denny, J. A.; Hall, M. B.; Darensbourg, M. Y. Regioselectivity in Ligand Substitution Reactions on Diiron Complexes Governed by Nucleophilic and Electrophilic Ligand Properties. *Inorg. Chem.* **2015**, *54*, 3523−3535. (f) Weber, K.; Weyhermueller, T.; Bill, E.; Erdem, O. F.; Lubitz, W. Design and Characterization of Phosphine Iron Hydrides: Toward Hydrogen-Producing Catalysts. *Inorg. Chem.* **2015**, *54*, 6928−6937. (g) Filippi, G.; Arrigoni, F.; Bertini, L.; De Gioia, L.; Zampella, G. DFT Dissection of the Reduction Step in H_2 Catalytic Production by [FeFe]-Hydrogenase-Inspired Models: Can the Bridging Hydride Become More Reactive Than the Terminal Isomer? *Inorg. Chem.* **2015**, *54*, 9529−9542. (h) Gloaguen, F. Electrochemistry of Simple Organometallic Models of Iron−Iron Hydrogenases in Organic Solvent and Water. *Inorg. Chem.* **2016**, *55*, 390−398. (i) Xu, T.; Yin, C.-J. M.; Wodrich, M. D.; Mazza, S.; Schultz, K. M.; Scopelliti, R.; Hu, X. A Functional Model of [Fe]-Hydrogenase. *J. Am. Chem. Soc.* **2016**, *138*, 3270−3273. (j) Song, L.-C.; Xu, K.-K.; Han, X.-F.; Zhang, J.-W. Synthetic and Structural Studies of 2-Acylmethyl-6-R-Difunctionalized Pyridine Ligand-Containing Iron Complexes Related to [Fe]-Hydrogenase. *Inorg. Chem.* **2016**, *55*, 1258−1269. (k) Seo, J.; Manes, T. A.; Rose, M. J. Structural and functional synthetic model of mono-iron hydrogenase featuring an anthracene scaffold. *Nat. Chem.* **2017**, *9*, 552−557. (l) Durgaprasad, G.; Xie, Z.-L.; Rose, M. J. Iron Hydride Detection and Intramolecular Hydride Transfer in a Synthetic Model of Mono-Iron Hydrogenase with a CNS Chelate. *Inorg. Chem.* **2016**, *55*, 386−389. (m) Yu, X.; Pang, M.; Zhang, S.; Hu, X.; Tung, C.; Wang, W. Terminal Thiolate-Dominated H/D Exchanges and H_2 Release: Diiron Thiol−Hydride. *J. Am. Chem. Soc.* **2018**, *140*, 11454−11463. (n) Rana, A.; Mondal, B.; Sen, P.; Dey, S.; Dey, A. Activating Fe(I) Porphyrins for the Hydrogen Evolution Reaction Using Second-Sphere Proton Transfer Residues. *Inorg. Chem.* **2017**, *56*, 1783−1793.

(8) (a) Lei, H.; Fang, H.; Han, Y.; Lai, W.; Fu, X.; Cao, R. Reactivity and Mechanism Studies of Hydrogen Evolution Catalyzed by Copper Corroles. *ACS Catal.* **2015**, *5*, 5145−5153. (b) Lei, H.; Li, X.; Meng, J.; Zheng, H.; Zhang, W.; Cao, R. Structure Effects of Metal Corroles on Energy-Related Small Molecule Activation Reactions. *ACS Catal.* **2019**, *9*, 4320−4344. (c) Haddad, A. Z.; Cronin, S. T.; Mashuta, M. S.; Buchanan, R. M.; Grapperhaus, C. A. Metal-Assisted Ligand-Centered Electrocatalytic Hydrogen Evolution upon Reduction of a Bis(thiosemicarbazonato)Cu(II) Complex. *Inorg. Chem.* **2017**, *56*, 11254−11265.

(9) (a) Eisenberg, R.; Gray, H. B. Noninnocence in Metal Complexes: A Dithiolene Dawn. *Inorg. Chem.* **2011**, *50*, 9741−9751. (b) Eisenberg, R. Trigonal Prismatic Coordination in Tris(dithiolene) Complexes: Guilty or just Non-innocent? *Coord. Chem. Rev.* **2011**, *255*, 825−836. (c) Ray, K.; Petrenko, T.; Wieghardt, K.; Neese, F. Joint Spectroscopic and Theoretical Investigations of Transition Metal Complexes involving Non-innocent Ligands. *Dalton Trans.* **2007**, 1552−1556. (d) Han, Z. H.; Eisenberg, R. Fuel from Water: The Photochemical Generation of Hydrogen from Water. *Acc. Chem. Res.* **2014**, *47*, 2537−2544. (e) Fourmigué, M. Mixed Cyclopentadienyl/dithiolene complexes. *Coord. Chem. Rev.* **1998**, *178*, 823−864. (f) Sproules, S.; Wieghardt, K. Dithiolene Radicals: Sulfur K-edge X-ray Absorption Spectroscopy and Harry's Intuition. *Coord. Chem. Rev.* **2011**, *255*, 837−860. (g) Sproules, S. Tris(dithiolene) Chemistry: A Golden Jubilee. *Prog. Inorg. Chem.* **2014**, *58*, 1−144.

(10) (a) McNamara, W. R.; Han, Z.; Yin, C.-J.; Brennessel, W. W.; Holland, P. L.; Eisenberg, R. Cobalt-dithiolene Complexes for the Photocatalytic and Electrocatalytic Reduction of Protons in Aqueous Solutions. *Proc. Natl. Acad. Sci. U. S. A.* **2012**, *109*, 15594−15599. (b) McNamara, W. R.; Han, Z.; Alperin, P. J.; Brennessel, W. W.; Holland, P. L.; Eisenberg, R. A Cobalt−Dithiolene Complex for the Photocatalytic and Electrocatalytic Reduction of Protons. *J. Am. Chem. Soc.* **2011**, *133*, 15368−15371. (c) Das, A.; Han, Z.; Haghighi, M. G.; Eisenberg, R. Photogeneration of Hydrogen from Water using CdSe Nanocrystals Demonstrating the Importance of Surface Exchange. *Proc. Natl. Acad. Sci. U. S. A.* **2013**, *110*, 16716−16723. (d) Downes, C. A.; Marinescu, S. C. Efficient Electrochemical and Photoelectrochemical H_2 Production from Water by a Cobalt Dithiolene One-Dimensional Metal−Organic Surface. *J. Am. Chem. Soc.* **2015**, *137*, 13740−13743. (e) Solis, B. H.; Hammes-Schiffer, S. Computational Study of Anomalous Reduction Potentials for Hydrogen Evolution Catalyzed by Cobalt Dithiolene Complexes. *J. Am. Chem. Soc.* **2012**, *134*, 15253−15256. (f) Letko, C. S.; Panetier, J. A.; Head-Gordon, M.; Tilley, T. D. Mechanism of the Electrocatalytic Reduction of Protons with Diaryldithiolene Cobalt Complexes. *J. Am. Chem. Soc.* **2014**, *136*, 9364−9376. (g) Panetier, J. A.; Letko, C. S.; Tilley, T. D.; Head-Gordon, M. Computational Characterization of Redox Non-Innocence in Cobalt-Bis(Diaryldithiolene)−Catalyzed Proton Reduction. *J. Chem. Theory Comput.* **2016**, *12*, 223−230. (h) Eady, S. C.; MacInnes, M. M.; Lehnert, N. Immobilized Cobalt Bis(benzenedithiolate) Complexes: Exceptionally Active Heterogeneous Electrocatalysts for Dihydrogen Production from Mildly Acidic Aqueous Solutions. *Inorg. Chem.* **2017**, *56*, 11654−11667. (i) Lee, K. J.; McCarthy, B. D.; Rountree, E. S.; Dempsey, J. L. Identification of an Electrode-Adsorbed Intermediate in the Catalytic Hydrogen Evolution Mechanism of a Cobalt Dithiolene Complex. *Inorg. Chem.* **2017**, *56*, 1988−1998.

(11) (a) Zarkadoulas, A.; Field, M. J.; Papatriantafyllopoulou, C.; Fize, J.; Artero, V.; Mitsopoulou, C. A. Experimental and Theoretical Insight into Electrocatalytic Hydrogen Evolution with Nickel Bis(aryldithiolene) Complexes as Catalysts. *Inorg. Chem.* **2016**, *55*, 432−444. (b) Gan, L.; Groy, T. L.; Tarakeshwar, P.; Mazinani, S. K. S.; Shearer, J.; Mujica, V.; Jones, A. K. A Nickel Phosphine Complex as a Fast and Efficient Hydrogen Production Catalyst. *J. Am. Chem. Soc.* **2015**, *137*, 1109−1115. (c) Das, A.; Han, Z.; Brennessel, W.; Holland, P.; Eisenberg, R. Nickel Complexes for Robust Light-Driven and Electrocatalytic Hydrogen Production from Water. *ACS Catal.* **2015**, *5*, 1397−1406. (d) Begum, A.; Moula, G.; Sarkar, S. A Nickel(II)−Sulfur-Based Radical-Ligand Complex as a Functional Model of Hydrogenase. *Chem. - Eur. J.* **2010**, *16*, 12324−12327. (e) Koshiba, K.; Yamauchi, K.; Sakai, K. Ligand-Based PCET Reduction in a Heteroleptic Ni(bpy)(dithiolene) Electrocatalyst Giving Rise to Higher Metal Basicity Required for Hydrogen Evolution. *ChemElectroChem* **2019**, *6*, 2273−2281.

(12) (a) Haddad, A. Z.; Kumar, D.; Sampson, K. O.; Matzner, A. M.; Mashuta, M. S.; Grapperhaus, C. A. Proposed Ligand-Centered Electrocatalytic Hydrogen Evolution and Hydrogen Oxidation at a Noninnocent Mononuclear Metal−Thiolate. *J. Am. Chem. Soc.* **2015**, *137*, 9238−9241. (b) Zhang, W.; Haddad, A. Z.; Garabato, B. D.; Kozlowski, P. M.; Buchanan, R. M.; Grapperhaus, C. A. Translation of Ligand-Centered Hydrogen Evolution Reaction Activity and Mechanism of a Rhenium-Thiolate from Solution to Modified Electrodes: A Combined Experimental and Density Functional Theory Study. *Inorg. Chem.* **2017**, *56*, 2177−2187.

(13) (a) Dilworth, J. R.; Hutson, A. J.; Morton, S.; Harman, M.; Hursthouse, M. B.; Zubieta, J.; Archer, C. M.; Kelly, J. D. The Preparation and Electrochemistry of Technetium and Rhenium Complexes of 2-(diphenylphosphino)benzenethiol. The Crystal and Molecular Structures of $[Re(2\text{-}Ph_2PC_6H_4S)_3]$ and $[Tc(2\text{-}Ph_2PC_6H_4S)_3]$. *Polyhedron* **1992**, *11*, 2151−2155. (b) Dilworth, J. R.; Zheng, Y.; Lu, S.; Wu, Q. Preparation and Characterization of a Novel Asymmetrically Oxidized Complex of 2-(diphenylphosphino)-benzenethiol with Ruthenium. The Crystal and Molecular Structure of $[Ru(2\text{-}Ph_2PC_6H_4S)\cdot(2\text{-}Ph_2PC_6H_4S{-}OH)(2\text{-}Ph_2PC_6H_4SO_2)]\cdot 1/2H_2O$. *Transition Met. Chem.* **1992**, *17*, 364−368.

(14) (a) Tang, H.; Guan, J.; Hall, M. B. Understanding the Radical Nature of an Oxidized Ruthenium Tris(thiolate) Complex and Its Role in the Chemistry. *J. Am. Chem. Soc.* **2015**, *137*, 15616−15619. (b) Tang, H.; Brothers, E. N.; Hall, M. B. The Distinctive Electronic Structures of Rhenium Tris(thiolate) Complexes, an Unexpected

Contrast to the Valence Isoelectronic Ruthenium Tris(thiolate) Complexes. *Inorg. Chem.* **2017**, *56*, 583−593.
(15) (a) Grapperhaus, C. A.; Ouch, K.; Mashuta, M. S. Redox-Regulated Ethylene Binding to a Rhenium-Thiolate Complex. *J. Am. Chem. Soc.* **2009**, *131*, 64−65. (b) Ouch, K.; Mashuta, M. S.; Grapperhaus, C. A. Metal-Stabilized Thiyl Radicals as Scaffolds for Reversible Alkene Addition via C−S Bond Formation/Cleavage. *Inorg. Chem.* **2011**, *50*, 9904−9914.
(16) (a) Cizek, J. On the Use of the Cluster Expansion and the Technique of Diagrams in Calculations of Correlation Effects in Atoms and Molecules. *Adv. Chem. Phys.* **2007**, *14*, 35−89. (b) Purvis, G. D.; Bartlett, R. J. A Full Coupled-Cluster Singles and Doubles Model: The Inclusion of Disconnected Triples. *J. Chem. Phys.* **1982**, *76*, 1910−1918. (c) Scuseria, G. E.; Janssen, C. L.; Schaefer, H. F., III An Efficient Reformulation of the Closed−shell Coupled Cluster Single and Double Excitation (CCSD) Equations. *J. Chem. Phys.* **1988**, *89*, 7382−7387. (d) Scuseria, G. E.; Schaefer, H. F., III Is Coupled Cluster Singles and Doubles (CCSD) more Computationally Intensive than Quadratic Configuration Interaction (QCISD)? *J. Chem. Phys.* **1989**, *90*, 3700−3703. (e) Pople, J. A.; Head-Gordon, M.; Raghavachari, K. Quadratic Configuration Interaction. A General Technique for Determining Electron Correlation Energies. *J. Chem. Phys.* **1987**, *87*, 5968−5975.
(17) Roos, B. O. The Complete Active Space Self-Consistent Field Method and its Applications in Electronic Structure Calculations. *Adv. Chem. Phys.* **2007**, *69*, 399−445.
(18) Frisch, M. J.; Trucks, G. W.; Schlegel, H. B.; Scuseria, G. E.; Robb, M. A.; Cheeseman, J. R.; Scalmani, G.; Barone, V.; Mennucci, B.; Petersson, G. A.; Nakatsuji, H.; Caricato, M.; Li, X.; Hratchian, H. P.; Izmaylov, A. F.; Bloino, J.; Zheng, G.; Sonnenberg, J. L.; Hada, M.; Ehara, M.; Toyota, K.; Fukuda, R.; Hasegawa, J.; Ishida, M.; Nakajima, T.; Honda, Y.; Kitao, O.; Nakai, H.; Vreven, T.; Montgomery, J. A., Jr.; Peralta, J. E.; Ogliaro, F.; Bearpark, M.; Heyd, J. J.; Brothers, E.; Kudin, K. N.; Staroverov, V. N.; Kobayashi, R.; Normand, J.; Raghavachari, K.; Rendell, A.; Burant, J. C.; Iyengar, S. S; Tomasi, J.; Cossi, M.; Rega, N.; Millam, J. M.; Klene, M.; Knox, J. E.; Cross, J. B.; Bakken, V.; Adamo, C.; Jaramillo, J.; Gomperts, R.; Stratmann, R. E.; Yazyev, O.; Austin, A. J.; Cammi, R.; Pomelli, C.; Ochterski, J. W.; Martin, R. L.; Morokuma, K.; Zakrzewski, V. G.; Voth, G. A.; Salvador, P.; Dannenberg, J. J.; Dapprich, S.; Daniels, A. D.; Farkas, O.; Foresman, J. B.; Ortiz, J. V.; Cioslowski, J.; Fox, D. J. *Gaussian 09*, revision D. 01; Gaussian, Inc.: Wallingford, CT, 2013.
(19) Becke, A. D. Density-functional Thermochemistry. III. The Role of Exact Exchange. *J. Chem. Phys.* **1993**, *98*, 5648−5652.
(20) Zhao, Y.; Truhlar, D. G. A New Local Density Functional for Main-group Thermochemistry, Transition Metal Bonding, Thermo-Chemical Kinetics, and Noncovalent Interactions. *J. Chem. Phys.* **2006**, *125*, 194101.
(21) (a) Becke, A. D. Density-functional Exchange-energy Approximation with Correct Asymptotic Behavior. *Phys. Rev. A: At., Mol., Opt. Phys.* **1988**, *38*, 3098−3100. (b) Lee, C.; Yang, W.; Parr, R. G. Development of the Colle-Salvetti Correlation-energy Formula into a Functional of the Electron Density. *Phys. Rev. B: Condens. Matter Mater. Phys.* **1988**, *37*, 785−789. (c) Perdew, J. P. Density-functional Approximation for the Correlation Energy of the Inhomogeneous Electron Gas. *Phys. Rev. B: Condens. Matter Mater. Phys.* **1986**, *33*, 8822−8824.
(22) Tao, J.; Perdew, J. P.; Staroverov, V. N.; Scuseria, G. E. Climbing the Density Functional Ladder: Nonempirical Meta−Generalized Gradient Approximation Designed for Molecules and Solids. *Phys. Rev. Lett.* **2003**, *91*, 146401.
(23) Chai, J.-D.; Head-Gordon, M. Systematic Optimization of Long-range Corrected Hybrid Density Functionals. *J. Chem. Phys.* **2008**, *128*, 084106.
(24) Chai, J.-D.; Head-Gordon, M. Long-range Corrected Hybrid Density Functionals with Damped Atom−atom Dispersion Corrections. *Phys. Chem. Chem. Phys.* **2008**, *10*, 6615−6620.
(25) (a) Zhou, Z.; Fu, A.; Du, D. Studies on Density Functional Theory for the Electron-transfer Reaction Mechanism between M−C_6H_6 and M+−C_6H_6 Complexes in the Gas Phase. *Int. J. Quantum Chem.* **2000**, *78*, 186−194. (b) Perdew, J. P.; Burke, K.; Wang, Y. Generalized Gradient Approximation for the Exchange-correlation Hole of a Many-Electron System. *Phys. Rev. B: Condens. Matter Mater. Phys.* **1996**, *54*, 16533−16539.
(26) (a) Perdew, J. P.; Burke, K.; Ernzerhof, M. Generalized Gradient Approximation Made Simple. *Phys. Rev. Lett.* **1996**, *77*, 3865−3868. (b) Ernzerhof, M.; Scuseria, G. E. Assessment of the Perdew−Burke−Ernzerhof Exchange-correlation Functional. *J. Chem. Phys.* **1999**, *110*, 5029−5036. (c) Adamo, C.; Barone, V. Toward Reliable Density Functional Methods without Adjustable Parameters: The PBE0Model. *J. Chem. Phys.* **1999**, *110*, 6158−6170.
(27) Peverati, R.; Truhlar, D. G. Screened-exchange Density Functionals with Broad Accuracy for Chemistry and Solid-state Physics. *Phys. Chem. Chem. Phys.* **2012**, *14*, 16187−16191.
(28) Zhao, Y.; Truhlar, D. G. The M06 Suite of Density Functionals for Main Group Thermochemistry, Thermochemical Kinetics, NonCovalent Interactions, Excited States, and Transition Elements: Two New Functionals and Systematic Testing of Four M06-class Functionals and 12 other Functionals. *Theor. Chem. Acc.* **2008**, *120*, 215−241.
(29) Boese, A. D.; Martin, J. M. L. Development of Density Functionals for Thermochemical Kinetics. *J. Chem. Phys.* **2004**, *121*, 3405−3416.
(30) Hay, P. J.; Wadt, W. R. Ab initio Effective Core Potentials for Molecular Calculations. Potentials for the Transition Metal Atoms Sc to Hg. *J. Chem. Phys.* **1985**, *82*, 270−283.
(31) Marenich, A. V.; Cramer, C. J.; Truhlar, D. G. Universal Solvation Model Based on Solute Electron Density and on a Continuum Model of the Solvent Defined by the Bulk Dielectric Constant and Atomic Surface Tensions. *J. Phys. Chem. B* **2009**, *113*, 6378−6396.
(32) (a) Andrae, D.; Haeussermann, U.; Dolg, M.; Stoll, H.; Preuss, H. Energy-adjusted Ab initio Pseudopotentials for the Second and Third Row Transition Elements. *Theor. Chim. Acta* **1990**, *77*, 123−141. (b) Martin, J. M. L.; Sundermann, A. Correlation Consistent Valence Basis Sets for Use with the Stuttgart−Dresden−Bonn Relativistic Effective Core Potentials: The Atoms Ga−Kr and In−Xe. *J. Chem. Phys.* **2001**, *114*, 3408−3420.
(33) (a) Grimme, S.; Antony, J.; Ehrlich, S.; Krieg, H. A Consistent and Accurate ab initio Parametrization of Density Functional Dispersion Correction (DFT-D) for the 94 Elements H-Pu. *J. Chem. Phys.* **2010**, *132*, 154104. (b) Goerigk, L.; Grimme, S. Efficient and Accurate Double-Hybrid-Meta-GGA Density Functionals—Evaluation with the Extended GMTKN30 Database for General Main Group Thermochemistry, Kinetics, and Noncovalent Interactions. *J. Chem. Theory Comput.* **2011**, *7*, 291−309.
(34) Werner, H. J.; Knowles, P. J.; Knizia, G.; Manby, F. R.; Schütz, M.; Celani, P.; Korona, T.; Lindh, R.; Mitrushenkov, A.; Rauhut, G.; Shamasundar, K. R.; Adler, T. B.; Amos, R. D.; Bernhardsson, A.; Berning, A.; Cooper, D. L.; Deegan, M. J. O.; Dobbyn, A. J.; Eckert, F.; Goll, E.; Hampel, C.; Hesselmann, A.; Hetzer, G.; Hrenar, T.; Jansen, G.; Köppl, C.; Liu, Y.; Lloyd, A. W.; Mata, R. A.; May, A. J.; McNicholas, S. J.; Meyer, W.; Mura, M. E.; Nicklass, A.; O'Neill, D. P.; Palmieri, P.; Pflüger, K.; Pitzer, R.; Reiher, M.; Shiozaki, T.; Stoll, H.; Stone, A. J.; Tarroni, R.; Thorsteinsson, T.; Wang, M.; Wolf, A. *MOLPRO*, version 2012, a package of *ab* initio programs; see http://www.molpro.net.
(35) Raamat, E.; Kaupmees, K.; Ovsjannikov, G.; Trummal, A.; Kütt, A.; Saame, J.; Koppel, I.; Kaljurand, I.; Lipping, L.; Rodima, T.; Pihl, V.; Koppel, I. A.; Leito, I. Acidities of Strong Neutral Brønsted Acids in Different Media. *J. Phys. Org. Chem.* **2013**, *26*, 162−170.

https://dx.doi.org/10.1021/acscatal.9b04579
ACS Catal. 2020, 10, 3778−3789